Monthly Notices of the ROYAL ASTRONOMICAL SOCIETY

MNRAS **511,** 4333–4349 (2022) https://doi.org/10.1093/mnras/stac331
Advance Access publication 2022 February 8

Cosmic Voids and BAO with relative baryon-CDM perturbations

Hasti Khoraminezhad,[1,2,3]★ Pauline Vielzeuf,[1,2] Titouan Lazeyras,[1,2,3] Carlo Baccigalupi[1,2,3,4] and Matteo Viel[1,2,3,4]

[1]*SISSA, Via Bonomea 265, I-34136 Trieste, Italy*
[2]*IFPU, Institute for Fundamental Physics of the Universe, via Beirut 2, I-34151 Trieste, Italy*
[3]*INFN, Sezione di Trieste, Via Bonomea 265, I-34136 Trieste, Italy*
[4]*INAF, Osservatorio Astronomico di Trieste, Via Tiepolo 11, I-34143 Trieste, Italy*

Accepted 2022 February 2. Received 2022 February 2; in original form 2021 September 15

ABSTRACT

We study the statistics of various large-scale structure tracers in gravity-only cosmological simulations including baryons and cold dark matter (CDM) initialized with two different transfer functions, and simulated as two distinct fluids. This allows us to study the impact of baryon-CDM relative perturbations on these statistics. In particular, we focus on the statistics of cosmic voids, as well as on the matter and halo real-space 2-point correlation function and baryon acoustic oscillations (BAO) peak. We find that the void size function is affected at the 1–2 per cent level at maximum, and that the impact is more important at higher redshift, while the void density profile and void bias are roughly unaffected. We do not detect a sizeable impact of relative baryon-CDM perturbations on the real-space correlation functions of matter and haloes or the BAO peak, which is in line with results from previous works. Our results imply that it would be hard to use voids or real-space correlation functions to constrain baryon-CDM relative perturbations, but also that we might not have to include them in models for the analysis of future cosmological surveys data.

Key words: galaxies: clusters: general – cosmology: theory – dark matter – large-scale structure of Universe.

1 INTRODUCTION

The different evolution of baryons and cold dark matter (CDM) due to photon pressure before recombination causes relative perturbations between the two fluids in the early Universe. These perturbations can be both in the density and peculiar velocity of the two fields but, importantly, they keep the total matter perturbations unchanged, and are thus referred to as relative baryon-CDM density perturbations and relative baryon-CDM velocity perturbations (Dalal, Pen & Seljak 2010; Tseliakhovich & Hirata 2010; Barkana & Loeb 2011; Yoo, Dalal & Seljak 2011; Yoo & Seljak 2013; Slepian & Eisenstein 2015; Blazek, McEwen & Hirata 2016; Schmidt 2016; Beutler, Seljak & Vlah 2017; Slepian et al. 2018; Khoraminezhad et al. 2021). After recombination, these primordial relative perturbations are slowly erased by gravitational evolution with baryons falling in CDM potential wells. In standard studies of Large-Scale Structure (LSS), this process is assumed to be complete before redshift zero, and baryons and CDM are treated as one single comoving matter fluid. However, this assumption is not exactly correct, and there were several recent efforts to describe the evolution of baryons and CDM as two distinct fluids across cosmic history (see in particular Tseliakhovich & Hirata 2010; Barkana & Loeb 2011; Schmidt 2016; Beutler et al. 2017; Chen, Castorina & White 2019; Rampf, Uhlemann & Hahn 2021). Notice that similar perturbations can also be generated in some inflationary scenarios, and are then referred to as Compensated Isocurvature Perturbations (CIPs) (Polarski & Starobinsky 1994; Linde & Mukhanov 1997; Langlois & Riazuelo 2000; Liddle & Mazumdar 2000; Notari & Riotto 2002; Lyth, Ungarelli & Wands 2003; Ferrer, Rasanen & Valiviita 2004; Li et al. 2009; Grin, Dore & Kamionkowski 2011; Valiviita et al. 2012; Christopherson 2014; Huston & Christopherson 2014; He, Grin & Hu 2015; Heinrich & Schmittfull 2019; Barreira et al. 2020b). However, in this work, we do not treat these CIPs, and we focus only on relative baryon-CDM perturbations induced by photon pressure prior to recombination.

2-fluid simulations in which baryons and CDM are initialized with two different transfer functions and are considered as two distinct fluids coupled gravitationally are starting to play an important role in this line of study (see Yoshida, Sugiyama & Hernquist 2003; O'Leary & McQuinn 2012; Angulo, Hahn & Abel 2013; Bird et al. 2020; Hahn, Rampf & Uhlemann 2021; Khoraminezhad et al. 2021; Michaux et al. 2021). Crucially, these are gravity-only simulations (i.e. they do not include any late-time hydrodynamics), and early-universe baryonic effects only enter through the use of different transfer functions to initialize baryons and CDM.

Relative velocity perturbations were identified for the first time by Tseliakhovich & Hirata (2010), while relative density perturbations were first pointed out in Barkana & Loeb (2011). In both cases, they are expected to affect structure formation (Ahn 2016), as well as the clustering of LSS tracers (Schmidt 2016; Beutler et al. 2017; Barreira et al. 2020a; Khoraminezhad et al. 2021). This is because the coupling of baryons to photons before recombination prevents baryons from evolving gravitationally together with CDM, and consequently acts against structure formation and clustering, an effect that might need

★ E-mail: hkhorami@sissa.it

to be taken into account in studies of LSS. The formalism to include baryon-CDM relative perturbations in the statistics of LSS tracers was first discussed in Schmidt (2016) using the bias formalism (see Desjacques, Jeong & Schmidt (2018) for a complete review on this formalism). The main point is the need to add new terms proportional to these relative perturbations to the bias expansion, which links the density of tracers such as haloes or galaxies δ_h to various underlying perturbations. At linear order, these terms consist of the relative density perturbation δ_{bc} (with $\delta_{bc} = \delta_b - \delta_c$) and relative velocity divergence perturbation θ_{bc} (with $\theta_{bc} = \theta_b - \theta_c$) multiplied by their respective bias parameters $b_{\delta_{bc}}$ and $b_{\theta_{bc}}$, and the overdensity of haloes can be written as (note that here $\mathbf{x}$, indicates the Eulerian position)

$$\delta_h(\mathbf{x}, z) = b_1(z)\delta_m(\mathbf{x}, z) + b_{\delta_{bc}}(z)\delta_{bc}(\mathbf{x}) + b_{\theta_{bc}}(z)\theta_{bc}(\mathbf{x}, z), \quad (1)$$

where b_1 is the standard linear bias. The parameters $b_{\delta_{bc}}$ and $b_{\theta_{bc}}$ were studied in previous works (see for example Barkana & Loeb 2011; Schmidt 2016; Beutler et al. 2017; Chen et al. 2019; Hotinli et al. 2019; Barreira et al. 2020a; Khoraminezhad et al. 2021). Specifically, Barreira et al. (2020a) used the separate universe simulations technique to do the first measurement of $b_{\delta_{bc}}$ (corresponding to CIPs generated during Inflation), while Khoraminezhad et al. (2021) measured $b_{\delta_{bc}}$ using gravity-only 2-fluid simulations (corresponding to relative perturbations generated by photon pressure), and showed the two parameters to be equal. This work is a follow-up of Khoraminezhad et al. (2021), and we will investigate the effects that such perturbations could induce on specific structures and cosmological probes. It is worth mentioning that one of the first usage of the separate universe technique for isocurvature perturbations appeared in Jamieson & Loverde (2019). This was done for the case of dark energy/CDM relative perturbations but is nevertheless somewhat related to the perturbations we consider here, and pioneered the use of separate universe simulations for isocurvature perturbations.

The first structures we consider are cosmic voids. Cosmic voids are defined as large underdense regions of the cosmic web, they are the largest structures in the Universe and make up most of its volume (Cautun et al. 2014; Falck & Neyrinck 2015). Historically, their existence was one of the earliest predictions of the concordance cosmological model (Hausman, Olson & Roth 1983), and their observational detection goes back to roughly 40 yr ago (Gregory, Thompson & Tifft 1978; Kirshner et al. 1981). Voids are in particular extremely underdense near their centres, and their spherically averaged density profile shows a characteristic shape (Colberg et al. 2005; Ricciardelli, Quilis & Planelles 2013; Hamaus, Sutter & Wandelt 2014a; Nadathur et al. 2014b; Ricciardelli, Quilis & Varela 2014). Recently, cosmic voids are becoming a promising cosmological probes: first they could represent a population of statistically ideal spheres with a homogeneous distribution at different redshifts which size evolution could be used to probe the expansion of the Universe using Alcock & Paczynski tests (Alcock & Paczynski 1979; Lavaux & Wandelt 2012; Sutter et al. 2012; Sutter et al. 2014b; Hamaus et al. 2015; Hamaus et al. 2016; Mao et al. 2017; Hamaus et al. 2022). Moreover, due to their low density, voids are naturally sensitive to dark energy and thus the interest to use them as probe of alternative Dark Energy models and modified gravity scenarios is increasing (Odrzywołek 2009; Lavaux & Wandelt 2010; D'Amico et al. 2011; Li 2011; Bos et al. 2012; Clampitt, Cai & Li 2013; Gibbons et al. 2014; Barreira et al. 2015; Cai, Padilla & Li 2015; Pisani et al. 2015; Zivick et al. 2015; Pollina et al. 2016; Baldi & Villaescusa-Navarro 2018), as well as the possibility of using them to put constraints on neutrinos masses (Massara et al. 2015; Kreisch et al. 2019; Contarini et al. 2021). Their imprint on the observed Cosmic Microwave Background (CMB) is also becoming an encouraging new cosmological probe, either through their Integrated Sachs-Wolfe (ISW) imprint (Baccigalupi, Amendola & Occhionero 1997; Baccigalupi 1999; Granett, Neyrinck & Szapudi 2008; Cai et al. 2014; Granett, Kovács & Hawken 2015; Hotchkiss et al. 2015; Ade et al. 2016; Nadathur & Crittenden 2016; Kovács et al. 2017; Kovács et al. 2019; Hang et al. 2021), or their lensing imprint (Cai et al. 2017; Raghunathan et al. 2020; Vielzeuf et al. 2021). Furthermore, the observed cold spot of the CMB could be explained as the imprint of the ISW sourced by very large voids along the line of sight (Rees, Sciama & Stobbs 1968; Kovac et al. 2013; Finelli et al. 2014; Nadathur et al. 2014a). Moreover, some works such as Jamieson & Loverde (2019) studied the properties of the voids via the separate universe technique. Finally, some studies tried to link high redshift intergalactic voids in the transmitted Lyman-α flux to the gas density (Viel, Colberg & Kim 2008). Because they are almost empty regions, their evolution during cosmic history is at most weakly non-linear and their properties could possibly be impacted by the primordial density fields from which they formed. This fact motivates us to investigate the effects of baryon-CDM relative perturbations on these objects and their statistics.

Secondly, we will consider the real-space correlation function of various fields in our simulations. We will in particular focus on the Baryon Acoustic Oscillation (BAO) feature. Measuring the BAO feature in the distribution of galaxies is one of the most powerful tools for precision cosmology. For instance, the latest cosmological implications from final measurements of clustering using galaxies, quasars, and Lyα forests from the Sloan Digital Sky Survey (SDSS) reported the following cosmological constraints: $H_0 = 68.20 \pm 0.81$ km s^{-1}Mpc^{-1} and $\sigma_8 = 0.8140 \pm 0.0093$ allowing for a free curvature and a time evolving equation of state for the dark energy (Alam et al. 2021). Furthermore, combining the full-shape and BAO analyses of galaxy power spectra of the final Baryon Oscillation Spectroscopic Survey (BOSS) data release, Philcox et al. (2020), recently obtained a 1.6 per cent precision measurement of H_0. Recent works suggest that relative baryon-CDM perturbations δ_{bc} and θ_{bc} could provoke possible systematics in the estimation of the BAO peak position (Dalal et al. 2010; Barkana & Loeb 2011; Yoo & Seljak 2013; Schmidt 2016; Beutler et al. 2017; Barreira et al. 2020a), and thus could potentially bias the cosmological constraints as a systematic shift in $D_A(z)$, $H(z)$, and $f\sigma_8$ measurements.

The goal of this paper is to assess the impact of relative baryon-CDM perturbations on one side cosmic voids, and on the other side on the real-space correlation functions of various fluids, in particular the position of the BAO peak. We do this using the aforementioned 2-fluid simulations, and compare the results with those obtained in a standard gravity-only 1-fluid simulations. We emphasis that we work in configuration space, in contrast with our first paper where we worked in Fourier space (Khoraminezhad et al. 2021). We first give a detailed description of our numerical arrangement in Section 2, including details of our simulation setup and the halo finding procedure (Section 2.1), as well as the void finding algorithm (Section 2.2). We then investigate the impact of baryon-CDM perturbations on the void size function (VSF) using different tracers of the underlying matter field to identify cosmic voids (namely particles and haloes) in Section 3. In Section 4, we measure the void–void and halo–void correlation functions (Section 4.1), the void density profile (Section 4.2), and the void bias (Section 4.3) in presence of baryon-CDM perturbations. We further explore the effect of such perturbations on the real-space matter and halo 2-point correlation functions (2PCF) in Section 5, and in particular, we compare the position of the BAO peak in the 2PCF of total matter,

Table 1. Principal parameters of our numerical setup. $L_{\rm box}$ denotes the length of the side of the box, N_b and N_c are the number of baryon and CDM particles, respectively, m_b and m_c denote their corresponding mass in units of $10^{10}M_\odot\,h^{-1}$, and $N_{\rm real}$ is the number of realizations.

Name	$L_{\rm box}$	N_b	N_c	m_b ($10^{10}M_\odot\,h^{-1}$)	m_c ($10^{10}M_\odot\,h^{-1}$)	$N_{\rm real}$
–	(Mpc h^{-1})	–	–			–
1-fluid	500	0	512^3	–	1.0051	8
2-fluid	500	512^3	512^3	0.1583	0.8468	8

haloes, CDM, baryons, and the relative density δ_{bc} in Section 5.2. Finally, we draw our conclusions in Section 6.

2 NUMERICAL SETUP

2.1 Simulations and halo finding

Our *N*-body simulation suite is based on the one presented in Khoraminezhad et al. (2021), and consists of

(i) a set of collision-less gravity-only simulations in which baryons and CDM are evolved as two distinct fluids initialized from two distinct primordial power spectra as predicted by early universe physics. We refer to this set of simulations as '2-fluid'.

(ii) a set of a standard gravity-only simulation in which the baryons and CDM are considered as perfectly comoving and are hence simulated as one total matter field. We refer to this set as '1-fluid'.

Our cosmology is consistent with Planck 2018 (Aghanim et al. 2020) ΛCDM, namely: $\Omega_m = 0.3111$, $\Omega_b = 0.0490$, $\Omega_c = 0.2621$, $\Omega_\Lambda = 0.6889$, $n_s = 0.9665$, $\sigma_8 = 0.8261$, and $h = 0.6766$. In this work, we enlarge our previous simulation box size to $L_{\rm box} = 500\ h^{-1}$ Mpc on each side to be large enough for void finding. We perform eight realizations of each types of simulations (1-fluid/2-fluid) with 512^3 particles of each species. Importantly, each realization was initialized with a different random seed but the seeds used for total matter in 1-fluid simulations are the same as the ones used for CDM in 2-fluid ones in order to minimize cosmic variance. The details of the simulations are given in Table 1.

To generate the initial conditions of the density and velocity perturbations we used the publicly available initial condition code 'MUSIC' (Hahn & Abel 2011) at redshift $z_i = 49$. For the 1-fluid case, we compute the matter power spectrum at $z = 0$ using the publicly available Boltzmann code CAMB (Lewis, Challinor & Lasenby 2000) and back-scale it to the initial redshift, while for the 2-fluid scenario we use the two different transfer functions for baryons and CDM directly at $z_i = 49$. We use the first-order Lagrangian perturbation theory, Zel'dovich approximation, (Zeldovich 1970) to estimate the velocity as well as the density fields. In order to reduce the effect of cosmic variance, we use the fixed-mode amplitude technique implemented in the MUSIC code (Angulo & Pontzen 2016). Importantly, we keep the total matter power spectrum the same for the 1-fluid and 2-fluid scenarios, and we use the same random seeds to initialize 1-fluid simulations and CDM particles in the 2-fluid case.

We perform our simulations using the cosmological *N*-body code GADGET-II (Springel 2005). In the case of 2-fluid simulations, as was discussed in Angulo et al. (2013), Khoraminezhad et al. (2021), since we have two different fluids (baryons as the light fluid and CDM as the heavy one), and a too high force resolution for a given mass resolution would lead to a spurious coupling between baryons and CDM, we use adaptive gravitational softening (AGS) (Iannuzzi & Dolag 2011) for baryons only, which allows the softening length to vary in space and time according to the local density, and alleviates the spurious coupling arising between CDM and baryon particles, as was discussed in Angulo et al. (2013), Khoraminezhad et al. (2021). In more details, in the 2-fluid simulation suite, the force affecting baryonic particles is softened adaptively using an SPH kernel with a size set by the 14th closest neighbours. Moreover we set the floor minimum softening length $\epsilon = 25h^{-1}$kpc, which corresponds to 1/40-th of the mean interparticle separation of the baryons. We note that the CDM softening length is kept constant through space and time to $\epsilon = 25h^{-1}$kpc, which corresponds to the 1/40-th of the mean CDM interparticle separation as well. These settings are tested and validated in details in Section 3.3 and Appendix B of Khoraminezhad et al. (2021). Finally, we insist again that since we are interested in computing the effect of early baryon-CDM perturbations on LSS, we neglect the late-time impact of baryonic processes and do not include hydrodynamical forces in the simulations. We refer the reader to Khoraminezhad et al. (2021) for all the details and validating tests of our numerical setup.

We use the spherical overdensity (SO) algorithm Amiga Halo Finder (AHF) (Gill, Knebe & Gibson 2004; Knollmann & Knebe 2009) to identify haloes. The definition of the virial radius is the one of a sphere in which the average density is given by $\bar{\rho}_{vir}(z) = \Delta_m(z)\,\rho_m(z)$, where ρ_m is the background total matter density. We chose the overdensity threshold as $\Delta_m = 200$, and set the minimum number of particles per halo to 20. For this work, we only used main haloes and discarded subhaloes from the catalogues. We identify haloes at redshift $z = 0$, $z = 0.5$, $z = 1$, $z = 1.5$, $z = 2$, and $z = 3$. In the case of 2-fluid simulations, we use both CDM and baryon particles to identify haloes. We compared the halo mass function in the 1-fluid and 2-fluid simulations and found good agreement (see fig. 3 of Khoraminezhad et al. 2021).

2.2 Void finder

We use the publicly available REVOLVER (REal-space VOid Locations from surVEy Reconstruction)[1] void finder to build our void catalogues with the ZOBOV (ZOnes Bordering On Voidness) algorithm (Neyrinck 2008), which is a 3D void finder and has been widely used both in simulations and observed catalogues (Nadathur et al. 2020; Contarini et al. 2021; Jeffrey et al. 2021). The ZOBOV algorithm performs a Voronoi tessellation of a set of points, identifies depressions in the density distribution of these points, and merges them into group of Voronoi cells using a watershed transform (Platen, van de Weygaert & Jones 2007) without pre-determined assumptions about voids shape, size, or mean underdensity, which is the most appealing aspect of the watershed method. Here we briefly outline the basic steps of the void-finding technique in ZOBOV and we refer the interested readers to the main ZOBOV paper (Neyrinck 2008) for a detailed description. One can describe the ZOBOV mechanism with the four following main steps:

(i) *Voronoi tessellation field estimator (Schaap 2007)*: the algorithm divides the space into cells around each tracer i (haloes or particles in this work) in which the region inside the cell is closer to particle i than to any other one. It then estimates the density of each Voronoi region using the volume of each cell $1/V(i)$.

(ii) *Definition of the minimum density*: after estimating the density in each cell in the first step, the algorithm finds the minimum density

[1] https://github.com/seshnadathur/Revolver

cells, defined as Voronoi cells with a density lower than all their neighbouring ones.

(iii) *Formation of basins*: the algorithm then joins adjacent higher density cells to the minimum-density cell until no neighbour cell with a higher density can be found. It means that the void finder links all the particles to their minimum density neighbour. This procedure defines basins as the zones of these cells. At this point, these basins themselves could be considered as voids because they are depression regions in the density field, but one single basin may also arise from spurious Poisson fluctuations due to the discreteness of the particles.

(iv) *Watershed transform*: the last step is when these basins are joined together using a watershed algorithm (Platen et al. 2007). For each basin b, the 'water' level is set to the minimum density of b. It is then slowly elevated so that it can flow to the neighbour basins, joining all of them to basin b. The process stops when the 'water' flows into a basin with a lower minimum, which defines the final void distribution.

Void centres are then defined as the centre of the largest sphere completely empty of tracer that can be inscribed within the void. Indeed, this is the best predictor of the location of the minimum of the matter density field (Nadathur & Hotchkiss 2015). The effective radius of the void, R_v, is computed using the total volume of the underdense region and assuming sphericity

$$V_{\rm void} \equiv \sum_{i=1}^{N} V_i^t = \frac{4}{3}\pi R_v^3, \tag{2}$$

where V_i^t is the volume of the Voronoi cell of the ith tracer, and N represents the number of points that are included in the void.

We run the ZOBOV algorithm for all realizations of our 1-fluid and 2-fluid simulations presented in Section 2.1 at redshift $z = 0$, $z = 0.5$, $z = 1$, $z = 1.5$, $z = 2$, and $z = 3$ for two tracers:

(i) Haloes
(ii) Dark matter particles.

In order to better handle the computational cost of running the void finder in the particle field, we have made a down-sampling routine to randomly select CDM particles of the simulation snapshots down to a constant average density of 6.71×10^6 particles per cubic box-size ($500\,h^{-1}$ Mpc), which corresponds to 5 per cent of the particles at each redshift, and insures us to be conservative with the density. We have verified that the different void statistics we study here were not affected when using a different random sample. We note that in the case of the 2-fluid simulation scenario, even if we have both types of particles (baryons & CDM) in the simulation, we only used the down-sampled positions of CDM particles. We should in principle select voids in the total matter density field, including baryons, however, the ZOBOV algorithm cannot discriminate between different populations of particles with different masses. Therefore, we must identify the voids in one of the two density fields only. Since CDM particles are much more massive than baryons, they are more representative of the underlying total mater field, and are the stronger contributor to the evolution of cosmic structures. We emphasize that we do not expect the inclusion of baryons or not in the void finding procedure to strongly affect our results.

We note that the total number of voids identified in the particle-field is significantly greater (from ∼20 times for $z = 0$ to ∼200 times for $z = 3$) than the number of voids in the halo field due to the difference in the mean tracer densities (Kreisch et al. 2019). Moreover, for both types of simulations when one uses haloes as tracer of the matter field, the total number of voids gradually decreases with increasing redshift (for instance for the 1st realization of our 1-fluid simulation we found 2085, 1950, 1621, 1225, 860, and 289 voids at $z = 0$, $z = 0.5$, $z = 1$, $z = 1.5$, $z = 2$, and $z = 3$, respectively) which is due to the fact that the number of haloes formed at higher redshift is smaller than the ones at lower redshift which decreases the tracer density at higher redshift, and consequently the number of voids. On the other hand, in the case where CDM particles are used as tracer, the total number of voids increases as the redshift increases since we kept the tracer density constant at all redshift in this case (for example, for the same 1st realization of the 1-fluid simulation in the particle field we found 32 544, 42 208, 52 188, 61 642, 70 076, and 83 430 voids at $z = 0$, $z = 0.5$, $z = 1$, $z = 1.5$, $z = 2$, and $z = 3$, respectively). In order to understand these features in the statistics of the voids in a better way, we will look at the distribution in size of cosmic voids in the next section.

3 VOID SIZE FUNCTION

The Void Size Function (VSF), or void abundance (Sheth & van de Weygaert 2004; Furlanetto & Piran 2006) is the number of voids in a given radius bin at a given redshift. The VSF is a relatively recent tool that nowadays is becoming promising to probe dark energy (Pisani et al. 2015; Verza et al. 2019) as well as constraining neutrino masses (Massara et al. 2015; Kreisch et al. 2019; Contarini et al. 2021). In addition to that, some recent works have also explored the differences between VSF in the concordance model of cosmology ΛCDM and modified gravity theories (see Cai et al. 2015), Galileon or non-local gravity (see Barreira et al. 2015), or the possibility of couplings between CDM and dark energy (see Pollina et al. 2016). Here we will present the comparison between the VSF in 1-fluid and 2-fluid simulations to assess the impact of baryon-CDM relative perturbations on these statistics. Each time we focus on voids identified both in the CDM density field (downsampled) and in the distribution of collapsed haloes to highlight how the use of different tracers with different bias might result in a different relative behaviour in the VSF. Notice that the impact of these perturbations has been studied in Khoraminezhad et al. (2021) for key observables of overdense regions of the density field (halo mass function and power spectrum, and the contribution of the baryon-CDM perturbation bias term to the halo power spectrum was found to be at maximum 0.3 per cent at $k = 0.1\,{\rm h\,Mpc^{-1}}$, at $z = 0$). However, they remain unexplored for underdense regions observables.

3.1 VSF in the halo field

The left-hand panel of Fig. 1 shows the void size function of voids identified in the halo field both for the 1-fluid (solid line) and 2-fluid (dashed line) simulations. Based on the fact that no relevant differences have been observed between the halo mass function of the two types of simulations (see fig. 3 of Khoraminezhad et al. 2021), we are not expecting the void size function to be strongly affected either. We do however notice that the number of small voids identified in the halo field in the 2-fluid simulation is higher than the one in the 1-fluid simulation for all redshifts considered, while for larger voids ($R_v \gtrsim 40\,{\rm Mpc\,h^{-1}}$) we can see the opposite trend (we identified more large voids in the 1-fluid simulation rather than the 2-fluid one). Nevertheless, these differences are relatively small and almost remain inside the errorbars (which shows the error on the mean obtained from the eight different realizations). This can be seen more directly in the lower left-hand panel of Fig. 1 that shows the ratio of the void size function in the 2-fluid and 1-fluid simulations. We see the most significant difference between 1-fluid and 2-fluid

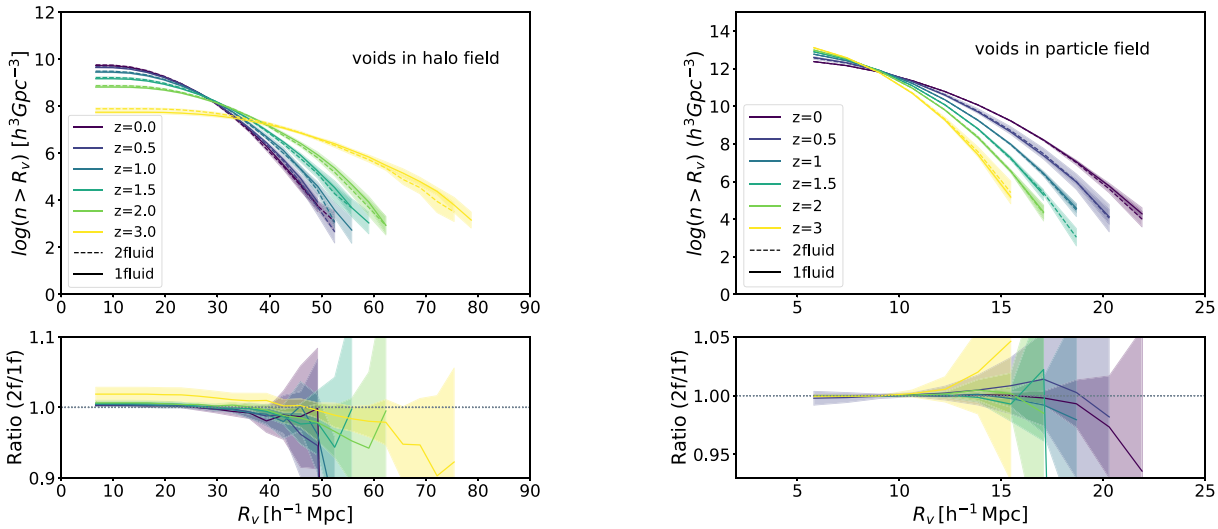

Figure 1. Cumulative void size function (number density of voids with radii above R_v) in the 2-fluid simulations in dashed and 1-fluid simulations in solid lines in the halo field (left-hand panel) and in the particle field (right-hand panel) for different redshift illustrated by the colour bar. The lower panels show the ratio of the VSF as '2-fluid/1-fluid' to see the difference better. The grey dotted line in the lower panels stand for the situation in which the VSF is equal in both types of simulations. The shaded area in each case depicts the 1σ error on the mean obtained from the eight different realizations.

simulations for small voids at $z = 3$, where we observe more small voids in 2-fluid simulations with a significance of roughly 1.5σ. We see the opposite effect for larger voids but with larger errorbars and consistent with 1. We emphasize the fact that the observed trend is something that we are expecting, since clustering is slightly diminished in 2-fluid simulations. Indeed, in Khoraminezhad et al. (2021), Fig. 9, we have shown that the amplitude of the ratio of the halo–halo power spectrum in 2-fluid simulation over the 1-fluid case is below 1, confirming the fact that baryon–photon coupling in the early universe decreases the clustering in 2-fluid simulations. Hence, we expect to have more small voids and less large voids in 2-fluid simulations, and we expect this effect to be more important at higher redshift since gravitational evolution washes out relative baryon-CDM perturbations after decoupling. We also note that the effect of baryon-CDM perturbations on the cumulative VSF is smaller than the effect caused by massive neutrinos (see for instance fig. 2 of Massara et al. (2015) in which the authors observed an impact due to neutrino masses up to ~ 30 per cent for $\sum m_\nu = 0.6\,\mathrm{eV}$ at $z = 0$). Finally, the left-hand panel of Fig. 1 shows that in both types of simulations, ZOBOV found more small voids at lower redshift and more large voids at higher redshift as can be seen in the redshift trend shown by the colour bar. This is also something that we expect, as discussed at the end of Section 2.2.

3.2 VSF in the particle field

The right-hand panel of Fig. 1 presents the VSF for voids found in the particle field. While we found more large voids and less small voids with increasing redshift in the case of halo field voids, here we see that we find more small voids at higher redshift (and symmetrically less large voids). The redshift trend, in this case, is hence different than for halo field voids for which we recall that the average density of tracers in the box is evolving with redshift which is not the case for particles. This confirms, as was shown in various previous works, that the void population depends on the tracer type one is using, in particular on the tracer density and tracer bias (see for example Sutter et al. 2014a; Contarini et al. 2019). The particle field voids are smaller and found in greater numbers than the voids in the halo field. This is due to the fact that the distribution of collapsed haloes is sparser than that of cold dark matter particles. These results are again expected, as we discussed at the end of Section 2.2.

For particle field voids, the difference in the number of voids found in the 1-fluid and 2-fluid simulations is even reduced compared to the halo field void case, and we do not observe any redshift evolution trend of the effect on these VSF caused by the 2-fluid formalism. Hence baryon–CDM relative perturbations impact the VSF of voids identified in haloes more importantly, which suggests that they might also impact the VSF of voids found using luminous tracers (such as galaxies) in observations.

4 VOIDS 2-POINT STATISTICS

We now move on to the 2-point statistics of voids, focusing first on the full correlation functions before analysing the voids profile and voids bias in more details.

4.1 Full correlation functions

The 2-point correlation function (2PCF) of a set of objects is a measurement of the degree of clustering of the considered objects defined as the excess probability of finding an object at a given distance from another one with respect to a homogeneous distribution of objects. Estimators of the 2PCF, $\xi(r)$, in which r denotes the comoving separation, have been studied by various authors (see for example Peebles & Hauser 1974; Hewett 1982; Davis & Peebles 1983; Hamilton 1993; Landy & Szalay 1993). Among them, we use the so-called 'natural' estimator (Peebles & Hauser 1974) which has been implemented in the nbodykit pipeline[2] (Hand et al. 2018) to measure the void and halo auto/cross 2PCF in our simulation boxes.

$$\xi(r) = \frac{DD(r)}{RR(r)} - 1, \tag{3}$$

[2]https://github.com/bccp/nbodykit

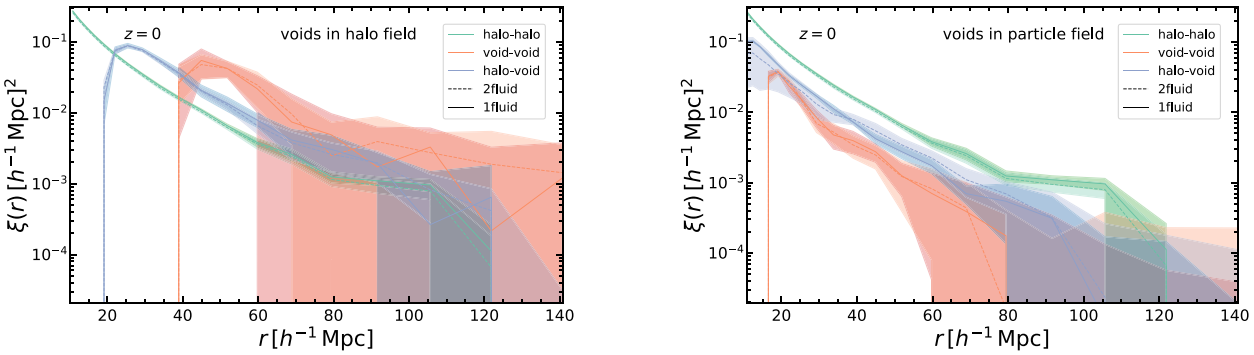

Figure 2. Void–void (orange), halo–halo (green), and halo–void (blue) 2PCF as a function of separation r using voids found in the halo field (left-hand panel) and the particle field (right-hand panel) at $z = 0$. The results for the 1- and 2-fluid cases are shown by solid and dashed lines, respectively. The shaded area in each case shows the 1σ error obtained from eight realizations.

which calculates the 2PCF using a data catalogue D, and a synthetic random catalogue R. $DD(r)$ and $RR(r)$ represent the pair counts with separation r in the data and random catalogues, respectively. Notice that, in order to reduce computational cost, nbodykit analytically estimates the random pairs $RR(r)$ in the case of uniform periodic randoms such as for simulated boxes.

Fig. 2 shows the void–void, halo–void, and halo–halo auto(cross)-correlation functions at $z = 0$ in 1- and 2-fluid simulations (solid and dashed lines, respectively), for voids identified both in the halo field (left-hand panel) and in the CDM particle field (right-hand panel). These correlations are computed for all haloes and voids without binning in size. For all cases, the 2PCF is monotonically decreasing as a function of distance. In both panels, the amplitude of the halo–void correlation function stands between the halo–halo and void–void ones for all separations r. The halo–halo correlation function (green curve) is the same in both panels (since it obviously does not depend on the tracer used to find voids), and serves as reference to compare the two cases. In the case of voids in the halo field, the amplitude of the halo–void and void–void cross/auto correlations is higher than the halo–halo case, while in the particle field, the halo–void and void–void 2PCFs are lower than the halo–halo one. This demonstrates that, as expected, voids identified in the halo field are more correlated with haloes than the voids found in the particle field. Another important feature here is that since voids are larger in the halo field than in the CDM particle field, the void–void 2PCF (orange curve) in the left-hand panel starts to be non-zero at larger separation than the one in the right-hand panel due to the exclusion effect. Indeed, since voids are low-density regions extending several tens of megaparsecs (hence with little amount of tracers inside them), the signal at scales inside the void radius becomes really low (or even zero) when computing the correlation function (or power spectrum) due to the lack of objects inside the voids, (see for instance Platen, van de Weygaert & Jones 2008; Chan, Hamaus & Desjacques 2014; Hamaus et al. 2014b). This also has for effect to increase the amplitude of the correlation on larger scales in the halo field since larger voids (corresponding to a merging of small ones) can form in the halo field. Finally, we further note that due to the much larger number of haloes in comparison to voids (~ 150 times larger) the signal to noise is much higher for the cross-correlation than the autocorrelation of voids. This for instance will have a consequence on the precision of the void bias estimation (see Section 4.3).

We now inspect in more details the impact of baryon-CDM relative perturbation on the 2PCFs by comparing results in the 1- and 2-fluid cases (solid versus dashed lines). We see that all differences are very small and well within 1σ errorbars. The largest difference is seen in the case of the halo–void correlation function for voids identified in the particle field (blue lines in the right-hand panel), with the 2PCF computed in the 2-fluid case being slightly smaller at small scales and slightly larger at larger scales. Moreover, we see a small trend on the halo–halo 2PCF, where the 2PCF computed using 2-fluid simulations seems always slightly below the one computed from 1-fluid simulations. This suggests that baryon-CDM relative perturbations tend to lower the clustering, which is in agreement with the expectation of baryon–photon coupling slowing down the clustering process (as discussed in Khoraminezhad et al. 2021). However, this effect is quite small and still within our errorbars. Note that this effect is also in agreement with the one we mentioned in Section 3.1 for the VSF, regarding the fact that since we have less clustering in 2-fluid simulations we identify more small voids and less large ones.

4.2 Density profiles

Cosmic voids are underdense regions close to their centre with an overdense compensation wall at $r \sim 2R_v$, r being the radial distance from the centre of the void. Moreover, the deepness of the void centre, as well as the amplitude of the compensation wall have been shown to strongly depend on the void population considered (see for example Ricciardelli et al. 2013; Hamaus et al. 2014a; Ricciardelli et al. 2014). The density profile of voids encodes the same information as the void-tracer cross-correlation function since the radial profile of voids is indeed equal to the way that we count the number of tracers at distance r from the centre of the void (see Hamaus et al. 2015; Pollina et al. 2017 for a detailed explanation). In more details, the average radial number density of tracers at distance r from the void centre, $\rho_{vt}(r)$ (also known in the literature as the void stacked profile), can be written as

$$\begin{aligned}\frac{\rho_{vt}(r)}{\langle\rho_t\rangle} &= \frac{1}{N_v}\sum_i \frac{\rho^i_{vt}(r)}{\langle\rho_t\rangle}\\ &= \frac{1}{N_v}\sum_i \frac{1}{N_t} V \sum_j \delta^D(x_i^{\rm center} - x_j^t + r)\\ &= V\sum_{i,j}\int \frac{1}{N_v}\delta^D(x_i^{\rm center} - x)\frac{1}{N_t}\delta^D(x - x_j^t + r)d^3x\\ &= \frac{1}{V}\int \frac{\rho_v(x)}{\langle\rho_v\rangle}\frac{\rho_t(x+r)}{\langle\rho_t\rangle}d^3x = 1 + \xi_{vt}(r),\end{aligned} \tag{4}$$

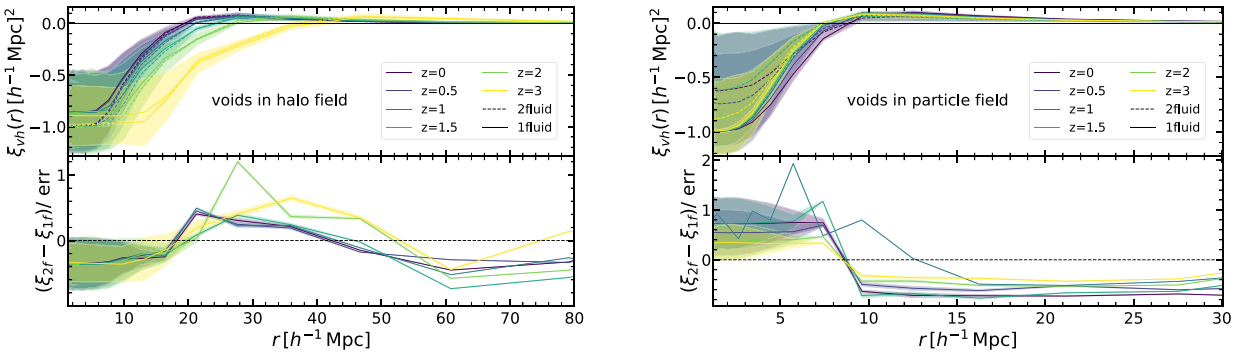

Figure 3. Halo–void cross-correlation corresponding to the void stacked profile for voids in the halo field (left-hand panel) and in the particle field (right-hand panel) at different redshift, and for 1-fluid and 2-fluid simulations (solid and dashed lines). We computed ξ_{vh} for all voids in our catalogues (i.e. without applying any cut in radius). Lower panels show the difference between 1-fluid and 2-fluid simulations over the parameter 'err', defined as $\mathrm{err} = \sqrt{\mathrm{err}^2_{\xi_{2f}} + \mathrm{err}^2_{\xi_{1f}}}$. Note that the curves at $z = 0$ are equivalent to the blue curves in Fig. 2, with a vertical axis in linear scale.

where N_v and N_t are the number of voids and tracers, respectively (with $\langle\rho_v\rangle$ and $\langle\rho_t\rangle$ their respective mean density), V is the total observed volume, x denotes the position (we use the index i to run over voids and j to run over tracers), and δ^D is the Dirac delta function. We have used the definition of the density of tracers within the void as a sum of Dirac deltas in the second equality, which can then be written as a convolution of the number density of the centre of the voids ρ_v and the number density of tracers ρ_t (third and fourth equality), which is finally the definition of the void-tracer cross-correlation function $\xi_{vt}(r)$.

We use this definition and compute the mean void profile as the halo–void cross-correlation function for voids identified both in the halo and particle field. The void density profile for different redshift and different simulations scenarios (1-fluid and 2-fluid) are presented in Fig. 3. The left-hand and right-hand panels display the density profiles of the voids identified in halo and particle fields, respectively. Note that Fig. 3 is similar to the blue curve in Fig. 2 but with a linear vertical axis, and for different redshift represented by the colour bar. In Fig. 3, we can distinguish three different scales with three different behaviours in the density profile:

(i) The innermost scales ($\sim r < \bar{R}_v/2$) ($\bar{R}_v$ is the mean void radius) in which ξ_{vh} approximately tends to -1 at the void centres. Note that since the central part of voids is not totally empty, the cross-correlation is not exactly equal to -1.

(ii) The intermediate scales ($\sim \bar{R}_v/2 < r < 2\bar{R}_v$) or the void profile regime, on which we can see the compensation wall of the voids, which is a positive correlation around the void at all redshift. Notice that for voids identified in the halo field (left-hand panel) the compensation wall moves to higher scales with increasing redshift. This is caused by the fact that the VSF at higher redshift is shifting towards larger radius voids (see Fig. 1, left-hand panel). On the contrary, in the case of particle field voids (right-hand panel), we see that the compensation wall moves towards lower scales with increasing redshift, which corresponds to the fact that the VSF of particle field voids at higher redshifts is shifting towards smaller radius voids (Fig. 1, right-hand panel).

(iii) The linear regime ($\sim r > 2\bar{R}_v$) in which we see that the compensation wall disappears and $\xi_{vh} \to 0$. This is the regime in which we will compute the void bias in Section 4.3.

Comparing the left-hand and right-hand panels of Fig. 3, we can also see that halo field voids have a much larger mean size than that of the particle field ones. This behaviour is confirmed by the VSF in Fig. 1. The bottom panels of Fig. 3 present the difference between 2-fluid simulations and the 1-fluid case over the error parameter which describes the quadrature summation of the errors in each case. We see that for the halo field voids, for small scales that are inside the void radius, the difference between the 2-fluid and 1-fluid correlation functions is slightly lower than zero at all redshifts, suggesting that 1-fluid voids are somewhat smoother (recall that the density is negative on those scales). This effect is within errorbars but can be seen for the mean value of the difference for halo field voids. Moreover, this effect is not seen in particle field voids (right-hand panel) due to the fact that the signal is more noisy since we correlate particle field voids with haloes. Finally, we note that errorbars in the void centre are quite large due to the low-density definition of voids, and thus the lower amount of haloes to compute the correlation.

The density profile of voids has been shown to depend on the void size (see for example Hamaus et al. 2014a; Sutter et al. 2014a), and we next explore whether or not the effect due to baryon-CDM perturbations could also vary with voids size. We divided our catalogues of void identified in the halo field in three different radius bins: $10 < R_v < 20\ h^{-1}\,\mathrm{Mpc}$, $20 < R_v < 30\ h^{-1}\,\mathrm{Mpc}$, $30 < R_v < 40\ h^{-1}\,\mathrm{Mpc}$, and the catalogues of void identified in the particle field in four radius bins: $1 < R_v < 5\ h^{-1}\,\mathrm{Mpc}, 5 < R_v < 10\ h^{-1}\,\mathrm{Mpc}, 10 < R_v < 15\ h^{-1}\,\mathrm{Mpc}$, $15 < R_v < 20\ h^{-1}\,\mathrm{Mpc}$. The void profile (i.e. the void–halo cross-correlation function) for each radius bin for each type of voids and at different redshift are shown in Fig. 4 (for halo field voids) and Fig. 5 (for particle field voids). In Fig. 4, we do not show results at $z = 3$ since the number of voids is quite small and the cross-correlation signal becomes too noisy. For both types of voids and for all different void size bins, we observe the same three different regimes mentioned above (the innermost scale, the intermediate scale, and the linear regime). We note that for all types of voids (found in haloes or particles) the compensation wall found at intermediate scales (the void profile regime) is more pronounced at smaller radius: in Fig. 4, we see a clear positive bump in the first panel for smallest halo field voids, and as we move to the second and third panels (to larger voids), the bump becomes less prominent and it disappears in the last panel for the largest voids. We observe the same behaviour in Fig. 5 for particle field voids. The results found here are qualitatively in agreement with Ceccarelli et al. (2013), Hamaus et al. (2014a) and Clampitt, Jain & Sánchez (2016).

In the same manner as for the void profiles of all voids (without classifying them by their radius), we show the difference of the results

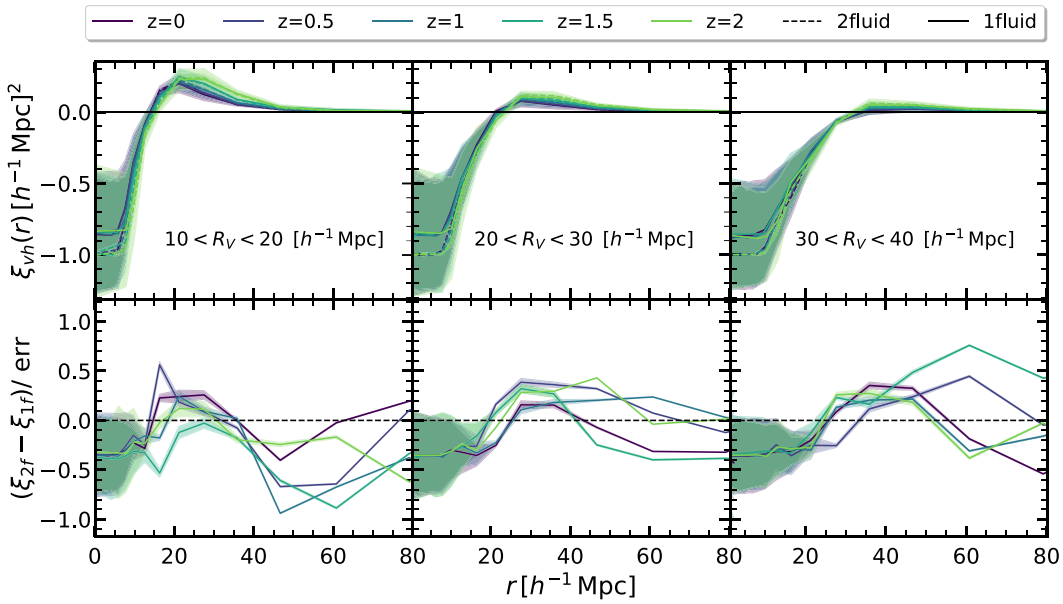

Figure 4. Void profile of halo field voids for three different bins of void radius R_v for 1-fluid (in solid line) and 2-fluid (in dashed line) simulations at five different redshift (colour coded). In each bin and at all redshift the cross-correlation approaches -1 close to the centre of the void ($\sim(r < R_v/2)$). On scales $\sim(R_v/2 < r < 2R_v)$, the void profile shows a prominent compensatory ridge of haloes for smaller voids $10 < R_v < 20\ h^{-1}$ Mpc, which disappears for the largest voids $30 < R_v < 40\ h^{-1}$ Mpc. In each bin, this compensation wall moves to lower radius (smaller voids) with decreasing redshift, which is the same behaviour as we noticed in Fig. 3. Lower panels show the difference between the 1-fluid and 2-fluid case over the error defined as $\mathrm{err} = \sqrt{\mathrm{err}^2_{\xi_{2f}} + \mathrm{err}^2_{\xi_{1f}}}$ for each void size bin, where we see that voids in the 2-fluid case tend to be slightly less dense in their centre.

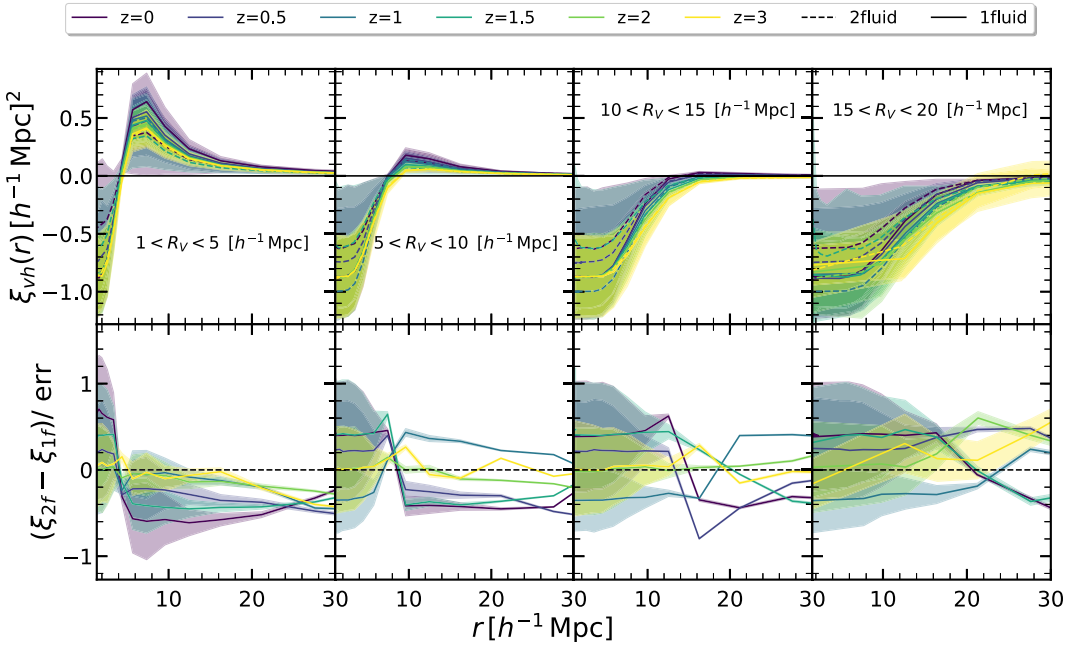

Figure 5. Same as Fig. 4 but for voids in the particle field in four different bins of void radius R_v. Since the number of voids identified in the particle field is larger than in the halo field, we divided them into more radius bins than halo field voids. The results of the 1-fluid scenario are shown by the solid lines and the ones of the 2-fluid by the dashed lines. The colour bar represent different redshift. The void profile shows a sizable compensation wall for the voids in the smallest size bin ($1 < R_v < 5\ h^{-1}$ Mpc). When moving to larger voids this structure becomes less prominent. The lower panels show the difference between the 1-fluid and 2-fluid case over the error defined as $\mathrm{err} = \sqrt{\mathrm{err}^2_{\xi_{2f}} + \mathrm{err}^2_{\xi_{1f}}}$ for each void size bin.

from the 2-fluid scenario and the 1-fluid one over the quadrature summation of the errors in each case in the lower panels of Figs 4 and 5. For halo field voids (Fig. 4), inside the voids, we see that $\xi_{vh,2f} < \xi_{vh,1f}$ at all redshift which tells us again that 1-fluid voids are slightly smoother. We do not observe this for particle field voids (Fig. 5), because the signal is much more noisy again. We note that the effect of baryon-CDM perturbations on void profiles does not seem to depend on the void radius as we observe that

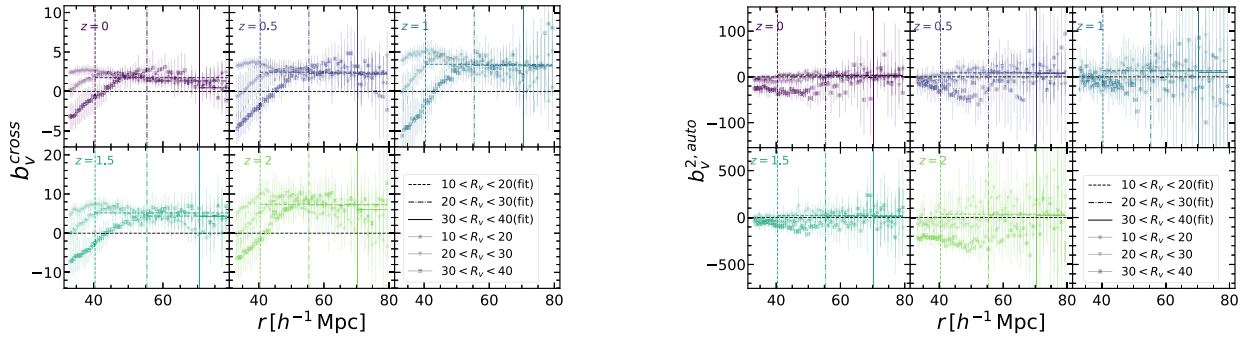

Figure 6. $b_v^{\rm cross}$ (left-hand panel) and $(b_v^{\rm auto})^2$ (right-hand panel) as a function of scale (equations 6–7) and an example of the fit with a zeroth order polynomial to obtain the mean void bias value. Both panels present results from 2-fluid simulations for voids in the halo field. Each subpanel with different colour presents results at a different redshift. Different markers and line styles show the measurement and associated fit at different void radius R_v. The vertical line in each line style is showing the $2R_v$ value for each bin. The errorbars show the 1σ error on the mean obtained from eight realizations. Since the number of voids is roughly $\sim$150 times less than the number of haloes, we have very large errors when computing $(b_v^{\rm auto})^2$.

the difference seems to be similar inside the voids in all panels. Finally, we emphasis that these differences are always compatible with 1 within 1σ errorbars, therefore we conclude that there are no significant differences between void profiles in 1-fluid and 2-fluid simulations, and hence that baryon-CDM relative perturbations due to photon pressure do not significantly impact this quantity. The results in each radius bin in Figs 4 and 5 are compatible with those obtained for all voids without binning in size (Fig. 3).

4.3 Void bias

In addition to the different void observables presented above, we also aim in this work to quantify the impact of baryon-CDM perturbations on the linear bias of cosmic voids. Indeed, the estimation of the clustering bias of cosmic voids is an essential element to achieve competitive cosmological inference from voids, in the same way as galaxy bias in the case of galaxies (Desjacques et al. 2018; Pezzotta et al. 2021; Schmidt 2021, and references therein). In this perspective, the interest in understanding it and modelling is raising (Sheth & van de Weygaert 2004; Chan et al. 2014; Hamaus et al. 2014b). Moreover, the possibility of using void bias directly to constrain cosmology is also recently gaining interest (see for example Chan, Hamaus & Biagetti 2019; Schuster et al. 2019; Chan et al. 2020). Here, we will measure the bias of our voids following the methodology described in Clampitt et al. (2016), for both 1-fluid and 2-fluid simulations at different redshift, and considering both voids identified in the halo field and in the particle field. Similarly to Clampitt et al. (2016), we define the void bias using two different expressions, the first one using the halo–void cross-correlation as

$$b_v^{\rm cross} = \frac{\xi_{vh}}{b_h\,\xi_{mm}}, \tag{5}$$

in which the halo bias can be obtain using the halo autocorrelation signal as $b_h \equiv \sqrt{\xi_{hh}/\xi_{mm}}$. Thus one can rewrite equation (5) as

$$b_v^{\rm cross} = \frac{\xi_{vh}}{\sqrt{\xi_{hh}\,\xi_{mm}}}. \tag{6}$$

The second definition uses the void–void autocorrelation as follows

$$b_v^{\rm auto} = \pm\sqrt{\frac{\xi_{vv}}{\xi_{mm}}}, \tag{7}$$

where in all the above equations ξ_{mm} is the matter–matter autocorrelation function measured directly from the simulation snapshots (using only CDM in 2-fluid simulations), and ξ_{hh} is the halo–halo autocorrelation function shown in Fig. 2. For $b_v^{\rm auto}$, we first measure the bias squared and then we chose the sign of the square root using the sign of $b_v^{\rm cross}$ (identically to what has been done in Clampitt et al. 2016). Considering the number of voids in each bin, we expect $b_v^{\rm auto}$ to be much more noisy. Nevertheless, it is interesting to cross-check to see if both bias measurements give comparable values.

Fig. 6 presents, as an example, the cross (left-hand panel) and auto (right-hand panel) bias as a function of scale for halo field voids at various redshift and void radius. Each small panel with different colour presents a different redshift. Considering the few number of voids identified at $z = 3$ and the low signal-to-noise ratio resulting, we do not show the bias analysis results at $z = 3$. We use different markers for different void size bins. The markers here show the mean value of the bias and the errorbars are the 1σ error over eight realizations. As expected, in the linear regime both bias are showing a constant behaviour. We then obtained the values for $b_v^{\rm cross}$ and $(b_v^{\rm auto})^2$ as a function of redshift and void size by fitting a zeroth order polynomial on linear scales (horizontal lines in the figure). In both cases, we use only scales between $2R_v < r(\mathrm{Mpc/h}) < 80$ for the fit. The lower limit assures that we are using only pairs of distinct voids, and the upper limit assures us to avoid the BAO scale on which dividing by ξ_{mm} would create a high noise. We use different line styles to show the fit in different size bins, and we show here the fit over the mean values taking into account the errorbars over different realizations. We also did the same fit for each of the realization to find the errorbars over the mean value of the bias from eight realizations. As expected, we observe a higher amount of noise in $(b_v^{\rm auto})^2$ than in $b_v^{\rm cross}$ (notice the difference in y-axis range) due to the fact that the pair counts in ξ_{vv} are much smaller than ξ_{vh}. In addition, the errorbars are increasing with redshift due to the smaller amount of voids found at higher redshift. Regarding the values of $b_v^{\rm cross}$ and $(b_v^{\rm auto})^2$, since the linear bias of haloes is increasing with redshift (e.g. Tinker et al. 2010), one can expect the voids identified with this tracer to also become less biased as time evolves, which is indeed what we observe. We also see that the void bias slightly decreases with increasing void size which is in agreement with the results in Clampitt et al. (2016), Hamaus et al. (2014b).

We then show in Fig. 7 the mean void bias as a function of the void radius integrated over the scales mentioned above (i.e. the value of the fits obtained on scales $2R_v < r < 80\,h^{-1}$ Mpc). We show both void bias results from cross-correlation, $b_v^{\rm cross}$, and autocorrelation $b_v^{\rm auto}$ using different tracers (in left-hand panels we present results in

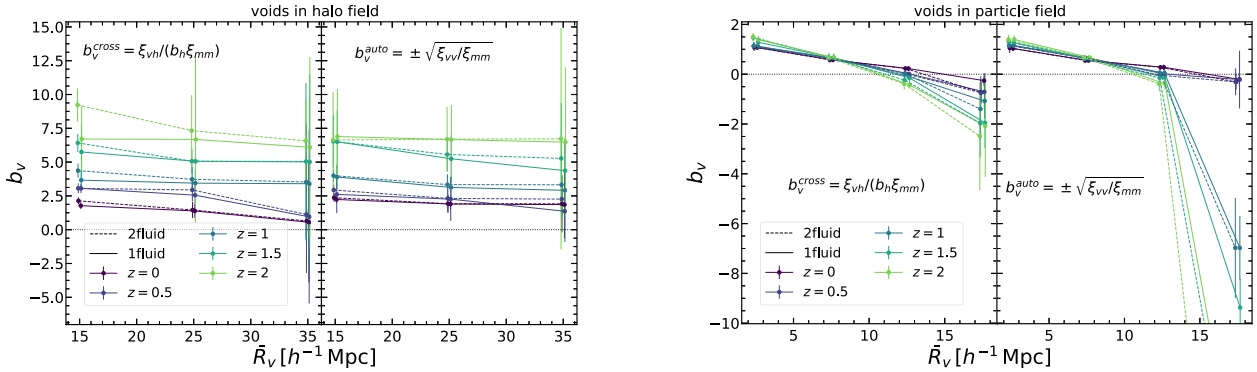

Figure 7. Mean, scale-independent void bias as a function of mean void radius $\bar{R}_v$ obtained from the fits on Fig. 6. Left-hand panels: $b_v^{\rm cross}$ and $b_v^{\rm auto}$ obtained using voids identified in the halo field for all different redshift (colour coded), for both 1-fluid (solid lines) and 2-fluid (dashed lines) simulations. We see that both $b_v^{\rm cross}$ and $b_v^{\rm auto}$ slightly decrease with increasing void size, and that both increase with increasing redshift. Right-hand panels: same as the left-hand panels but for voids found in the CDM particle field. In this case, we see that both biases depend more strongly on the void radius, and larger voids become negatively biased at all z. We further see that all voids become more positively bias and more negatively biased with increasing redshift. We observe only small differences that are all within 1σ errorbars between the void bias measured from 1- and 2-fluid simulations.

the halo field and the right-hand panels show results in the particle field). Different colours show different redshift as before. Since in the particle field we have a much larger number of voids, the errorbars are quite smaller compared to the halo field results. Moreover, the number of voids in both halo and matter fields drops significantly with increasing redshift, resulting in more noisy correlation measurement, and consequently, the errorbars of our void bias measurement are also increasing with redshift. This is the main reason why we do not show results at $z = 3$.

Inspecting Fig. 7 in more details, we see that measurements of the bias from the two definitions, i.e. using either the auto (equation 7) or the cross (equation 6) correlation signals, are broadly consistent for all void size bins considered, both for halo field and for particle field voids, except for the highest radius bin of the particle field voids. However, this is probably due to the fact that the signal in this case is really noisy due to the low number of objects, which affects our measurements and might lead to a slight underestimation of the errorbars. A detailed investigation is beyond the scope of this work in which we focus on the comparison between 1- and 2-fluid simulations. If we now inspect the difference between halo field and particle field voids, we see that choosing different tracer significantly affects the void bias: voids identified in the halo field are more biased than the particle field voids which is something expected since dark matter haloes are biased themselves. Furthermore, we find that in the case of the voids in the halo field, the mean value of the void bias is a slightly decreasing function of the void size (almost consistent with a constant considering the errorbars), while for the particle field, the void bias is a decreasing function as the size of the voids is increasing. In the right-hand panel of Fig. 7, we observe that the particle field void bias changes sign at a specific 'turning scale', which is a similar behaviour as observed by Clampitt et al. (2016), with however a different turning scale. This turning scale is roughly at $\sim 15\,h^{-1}$ Mpc for our voids in the particle field while roughly at $\sim 25\,h^{-1}$ Mpc for SDSS voids in Clampitt et al. (2016). However, we do not expect to observe the change of sign at the exact same scale since these authors find voids in a different tracer field using a different void finder.

Comparing the void bias from 1-fluid and 2-fluid simulations (solid versus dashed lines), we see that voids from the 2-fluid simulations are slightly more biased for both voids from the halo field and the particle field. This difference is within 1σ errorbars, but the trend of the 2-fluid simulation bias being slightly larger is expected: since the 2-fluid halo–halo 2PCF (the green curves in Fig. 2) is showing less clustering than in the 1-fluid scenario, the linear halo bias b_h is expected to be smaller in 2-fluid simulations as well. Then we can see from equations (5)–(7) that the void bias should be slightly larger in the 2-fluid case.

5 BARYON ACOUSTIC OSCILLATIONS

In this section, we extend the computation of the real-space 2-point correlation function in 2-fluid simulations from voids to each component of the simulations, i.e. total matter, baryons only, CDM only, baryon-CDM relative perturbations (δ_{bc}), and haloes. In particular, we focus on modulations of the BAO feature and BAO peak position by comparing our results for the total matter and halo fields in 1- and 2-fluid simulations. This is a direct extension of our previous work (Khoraminezhad et al. 2021) where we focused on Fourier space quantities.

Relative velocity perturbations between baryons and CDM can possibly shift the BAO scale because they are sourced by the same physical effect which imprinted the BAO peak itself. The shift in the BAO scale is crucial for cosmology since it could lead to a potential systematic shift in measurements of the angular diameter distance $D_A(z)$, the Hubble factor $H(z)$, and the growth factor $f\sigma_8$ (Dalal et al. 2010; Yoo & Seljak 2013; Beutler et al. 2017; Barreira et al. 2020a). This effect might also be important to obtain unbiased results when one is investigating the effect of massive neutrinos on the BAO scale (Peloso et al. 2015) or when one is using reconstruction methods to measure the BAO location in 21 cm intensity mapping surveys (Obuljen et al. 2017; Villaescusa-Navarro, Alonso & Viel 2017).

5.1 Full-shape correlation function

In this subsection, we first focus on the full shape of the 2-point correlation function. To compute the 2-point correlation function in real-space, we use the Fast Fourier Transform (FFT) estimator introduced in Taruya et al. (2009) in which the density field is computed on a grid in Fourier space, squared, inverse Fourier transformed, and averaged in radial bins

$$\xi_{\rm SIM}(r) = \frac{1}{N_{\rm modes}} \sum_{r_{\rm min}<|r|<r_{\rm max}} {\rm FFT}^{-1}\left[|\delta({\rm k})|^2\right]({\rm r}), \tag{8}$$

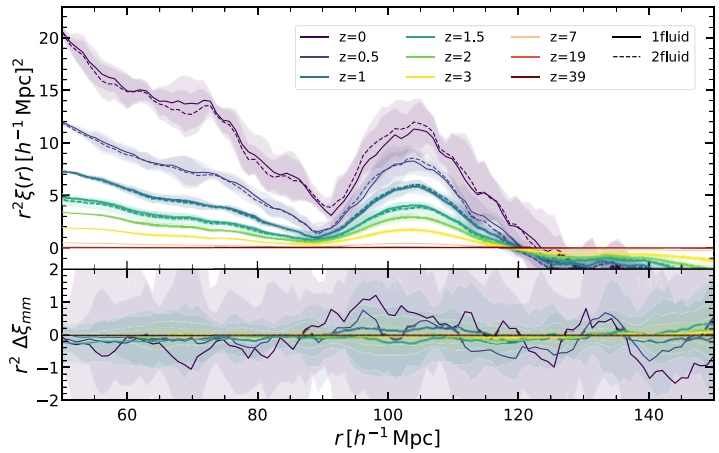

Figure 8. The redshift evolution of the full-shape total matter 2-point correlation function in 1-fluid (solid) and 2-fluid (dashed) simulations in real space as measured by equation (8). We multiply the 2PCF by r^2 to see the BAO peak better. The shaded area show the 1σ errorbar on the mean obtained from the standard deviation over all realizations. The lower panel presents the difference between 2-fluid and 1-fluid sets: $r^2\ \Delta\xi_{mm} = r^2\,(\xi^{2\mathrm{f}}_{mm} - \xi^{1\mathrm{f}}_{mm})$. We see that any small difference between the two cases is within the errorbars on all scales.

where the sum runs over all radii r in the bin and N_{modes} is the number of modes in the bin. We use the Cloud-In-Cell (CIC) mass-assignment scheme to compute the density field on the Fourier grid $\delta(k)$. To compute the total matter field δ_m in 2-fluid simulations is given by the weighted sum of the CDM field δ_c, and the baryon field δ_b, as δ_m as $\delta_m = f_b\delta_b + (1 - f_b)\delta_c$, where $f_b = \Omega_b/\Omega_m$. Moreover, we choose the edges of the bins r_{min} and r_{max} such that each bin as a width given by the mean interparticle separation, which in our case is $512\,h^{-1}\,\mathrm{Mpc}/500 \approx 1\ h^{-1}\,\mathrm{Mpc}$. We take advantage of the fact that this estimator is implemented in the PYLIANS library,[3] which we use to obtain our results. Finally, we restrict ourselves to the real-space 2-point correlation function in 1-fluid and 2-fluid simulations without considering redshift space. The estimator introduced here to calculate the 2PCF is much faster than the natural estimator we were using to compute the void correlation functions and density profiles in Section 4. There we were using the natural estimator since the sparsity of voids and exclusion effects introduce large noise which prevented us to use the Taruya estimator to obtain the void profile. Here, since we are interested in the correlation function of particles and haloes, which are by far more numerous, we can use the FFT estimator to significantly reduce the computation time while keeping a high-level of accuracy.

Fig. 8 shows the total matter–matter 2PCF computed in 1- and 2-fluid simulations (solid and dashed lines, respectively) using equation (8) for different redshift (colour coded). We recognize the standard shape of the correlation function which decreases as r increases, as well as the BAO peak at around $r \sim 105\,h^{-1}\,\mathrm{Mpc}$. We also see that both the correlation and the BAO peak increase with decreasing redshift since the clustering becomes more important at lower redshift. We observe small differences between the two cases with the correlation function being slightly lower on smaller scales in 2-fluid simulations, while on the scales of the BAO peak, the 2-fluid simulations give us a higher value of the 2PCF, and the effect is more important at low redshift due to non-linear evolution (recall that the total matter linear power spectrum is kept constant between 1- and 2-fluid simulations). Notice that these differences are within 1σ errorbars obtained over different realizations on all scales. These results confirm that baryon-CDM relative perturbations have a rather small impact on the matter clustering (under the detection threshold corresponding to our simulation volume) as was already pointed out in Angulo et al. (2013), Khoraminezhad et al. (2021).

We now turn to a more detailed investigation of the cross-correlation of each fluid component in 2-fluid simulations in Fig. 9. The top and middle panels show the two different component of the matter field (baryon and CDM) 2PCF divided by the square of the linear growth factor D^2. In case of baryons, we can see that the correlation function exhibits a strong BAO peak at high redshift, and that then the amplitude of the peak decreases with redshift due to gravitational interactions with CDM particles (note that with decreasing redshift the 1σ error on the mean value increases). We checked that the evolution of the baryon–baryon and CDM–CDM correlation functions, without multiplying by $D^{-2}(z)$, is the same as the total matter one (Fig. 8). Multiplying the baryon–baryon and CDM–CDM correlation functions by $D(z)^{-2}$ effectively removes the linear growth of structure and hence leaves only the fact that the BAO peak decreases with time. We can also see a small scale-dependent suppression of the correlation function at scales $r \lesssim 80\,h^{-1}\,\mathrm{Mpc}$ to accommodate for the growing peak. We see a somewhat different behaviour for CDM in the middle panel of Fig. 9: from $z = 39$ to $z = 7$, we see the BAO peak slightly increasing as CDM particles fall in the baryon potential well on these scales, imprinting the feature from the baryon field into the CDM field gradually (note that we observe the same position of the peak in baryons and CDM). The peak reaches its maximum relative amplitude at roughly $z = 7$, the moment at which mild non-linear effects appear. At redshift lower than $z = 7$, we observe then a small decrease in the peak amplitude. On small scales, we note the same scale-dependent suppression for CDM fluctuations that appeared as well in the baryon fluctuations. The results here are in agreement with the ones in fig. 9 of Angulo et al. (2013). In addition, as we saw for the halo–halo 2PCF in Fig. 2 (green curves), and also for the halo–halo power spectrum in fig. 9 of Khoraminezhad et al. (2021), baryon-CDM relative perturbations tend to diminish the clustering. We however observed a slight increase of clustering on scales around the position of the BAO peak in the matter–matter 2PCF in Fig. 8. We can now understand this in light of Fig. 9: the pronounced baryon BAO feature increases the total matter BAO peak in 2-fluid simulations.

[3] https://github.com/franciscovillaescusa/Pylians

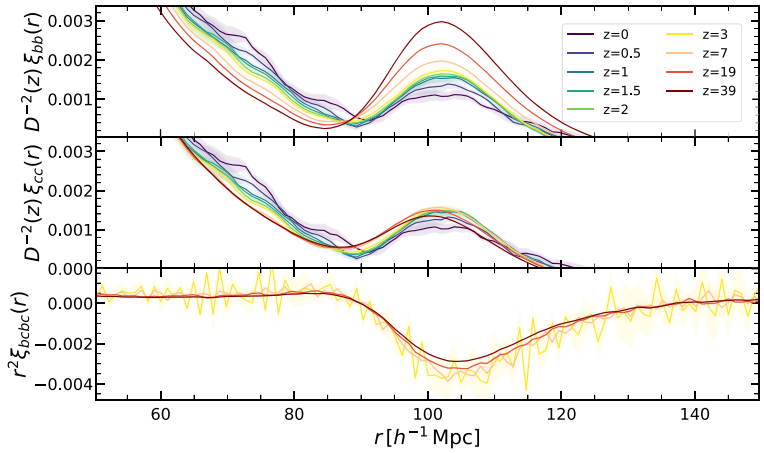

Figure 9. Top panel: Baryon 2-point correlation function measured in the 2-fluid simulations at different redshift (colour coded). We see clearly how the BAO peak of the baryon 2-point correlation function scaled by $D^{-2}(z)$, diminishes with time in this field. Middle panel: Same as top panel but for the CDM fluid. In this case and in this range of z, the BAO peak of the CDM 2-point correlation function scaled by $D^{-2}(z)$, remains roughly constant. We note that the evolution of the baryon–baryon and CDM–CDM correlation functions, without multiplying by $D^{-2}(z)$, is the same as what we have shown in Fig. 8 which is representing the total matter correlation function. Bottom: The δ_{bc} relative perturbation autocorrelation function. In this case, we show results down to $z = 3$ only since the noise becomes too important at later times. The BAO feature is clearly visible and is negative in this field. Furthermore, we see no redshift evolution, which is consistent with the fact that δ_{bc} is constant in time, as discussed in e.g. Schmidt (2016), Hahn et al. (2021), Khoraminezhad et al. (2021). Note that the two upper panels are divided by the square of the growth factor $D^2(z)$ to see the difference in evolution of BAO in baryons and CDM, while in the bottom panel we multiplied the 2PCF of δ_{bc} by r^2 in order to show the BAO feature better. The shaded area on each curve represent the 1σ error, and we see that with increasing redshift the error becomes less prominent.

Finally, we compute the 2-point correlation function of the baryon-CDM perturbation field δ_{bc} in the bottom panel of Fig. 9. We show this 2PCF only down to redshift $z = 3$ because the noise increases as we reach lower redshift, and the 2PCF becomes consistent with zero on all scales. We see that this 2PCF is roughly constant close to zero, except for the BAO feature which is a BAO dip instead of the BAO peak in this case. This is because the BAO feature in the baryon field gradually imprints itself into the CDM field, which creates a skewed distribution of CDM with a sharp fall inside the BAO scale but with a larger tail on scales slightly larger than the BAO one (even though the position of the BAO peak is observed to be identical for baryons and CDM). Therefore we expect to observe an anticorrelation signal for δ_{bc} on scales slightly larger than the BAO scale (δ_{bc} is too small) in a skewed way, as can be seen in the bottom panel of Fig. 9. We do not observe any notable redshift evolution for this 2PCF which is consistent with the fact that δ_{bc} itself is constant in time, as discussed in e.g. Schmidt (2016), Hahn et al. (2021), Khoraminezhad et al. (2021). Notice that this kind of correlation function was also predicted using 2LPT in Chen et al. (2019). While we do not conduct a detailed quantitative comparison of their prediction with our results, we note that they found the same kind of dip for correlation functions including relative baryon-CDM density perturbations.

Finally, we investigate the halo–halo 2PCF at redshift zero in Fig. 10. We present results for two halo mass bins centred around $\log M = 12.2 M_\odot\ h^{-1}$ and $\log M = 12.7 M_\odot\ h^{-1}$. Recall that haloes in the 2-fluid simulations are identified by considering both types of particles (baryons and CDM). As we see the halo–halo 2PCF is more noisy than the one obtained from particles due to the lower number of haloes in comparison to particles. We see that results obtained in the 2-fluid simulations are fully consistent with the ones from 1-fluid simulations. This once again reflects the smallness of the impact of baryon-CDM perturbations on galaxy clustering at low redshift and implies that these effects will probably not need to be included in the modelling of correlation functions for the analysis of future surveys BAO peak estimation. This has a positive impact for such analysis since it will reduce the number of free parameters entering the model. These results are in line with previous results in the literature: Barreira et al. (2020a), Khoraminezhad et al. (2021) estimated that the impact of baryon-CDM perturbations on the late-time halo power spectrum should not exceed 1 – a few per cent; Beutler et al. (2017) conducted an analysis of the BOSS DR12 data with a model including baryon-CDM relative density and velocity perturbations, and obtained results for the bias parameters associated with such perturbations consistent with zero, indicating an effect too small to be detected; finally, using 2LPT, Chen et al. (2019) showed the effect to be at most one order of magnitude smaller than the halo 2PCF itself.

5.2 Position of the BAO peak

We now focus more specifically on the position of the BAO peak estimation for our two sets of simulation. Anselmi et al. (2018) showed that the position of the BAO linear point, namely the midpoint scale between the peak and the dip of the 2PCF, can be extracted from the 2PCF measured in N-body simulations or galaxy data sets in a model-independent way by introducing a polynomial function to smooth the 2-point correlation function, and using a root-finding algorithm to estimate the zero-crossing of the first derivative of the 2PCF. To measure the linear point one needs to estimate the position of the BAO peak as well as the BAO dip through this modelling, but here we will just focus on the maximum of this fit. We use the following polynomial fit

$$\xi^{\mathrm{fit}}(r) = \sum_{n=0}^{N} a_n r^n. \tag{9}$$

Following Anselmi et al. (2018), we obtain the best-fitting parameter for the degree of the polynomial N by minimizing the χ^2. We use scales in the range $85 - 115\,h^{-1}$ Mpc, and we choose $N = 7$,

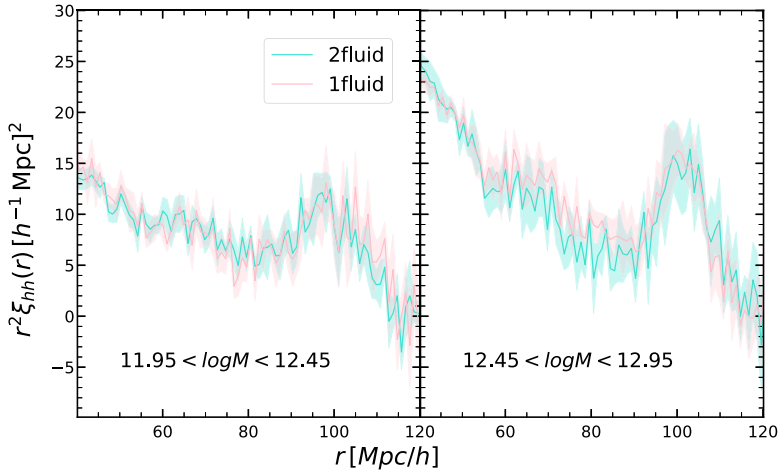

Figure 10. Halo–halo 2-point correlation function at $z = 0$ for 1-fluid (in pink) and 2-fluid (in blue) simulations for two different halo mass bins. The shaded area show the 1σ error over eight realizations of each set of simulations. Again we multiply the 2PCF by r^2 to better see the BAO feature. We do not detect any impact of baryon-CDM relative perturbations on this 2PCF either.

which allows us to obtain good fits in the sense that the reduced χ^2 is close to 1 for all correlation functions we consider here while avoiding overfitting. We have also checked that the results for the position of the BAO peak depend only weakly on the degree of the polynomial (for example, the results for the matter–matter correlation function are consistent for polynomials of degree 4 to 8). Having the polynomial fit, to identify the peak position, we find the point the fit where the first derivative of the 2PCF is equal to zero, and the second derivative is negative.

Fig. 11 illustrates this process by showing the matter–matter, CDM–CDM, and baryon–baryon correlation functions, and the related position of the BAO peak in each case (dotted-dashed vertical line with 1σ error) at $z = 0$. Each time the solid line shows the measurement while the dashed line shows the fit. We see that the position of the peak extracted from the baryon–baryon and CDM–CDM 2PCFs align with each other and with the total matter one in 2-fluid simulations. The position of the peak in 1-fluid simulation is slightly higher but the difference between the two cases lies within the 1σ errorbars. As we explained in the discussion of Fig. 9, this is expected since the BAO feature originates in the baryon field through baryon oscillations sourced by photon pressure, and then is imprinted into the CDM field with the same position but a lightly skewed distribution towards higher values. This results in a slightly overestimated position of the peak when assuming that the two fluids perfectly comove as is done in 1-fluid simulations.

The values of the position of the BAO peak for each fluid and for several redshift are reported in Table 2 as well as in Fig. 12 in details. Fig. 12 shows the 2-fluid measurements in nuances in blue for different fields and the 1-fluid case in red. We note that in the case of bcbc we show the position of the BAO dip both in Fig. 12 and Table 2. Since the position of the BAO peak in all cases remains the same within errorbars (at least with the eight realizations that we used here), we can argue that the BAO peak remains a standard ruler even in the presence of baryon-CDM perturbations. Notice that to decrease the errorbars by at least a factor of 5, we would need at least 900 realizations of each types of simulations but this would still not assure that we would see any significant differences.

Using the results in Fig. 10, we also computed the BAO peak position in the halo–halo 2-point correlation function for 2-fluid and 1-fluid simulations for the high mass bin. The results are shown in the last column of Table 2. As was already visible in the left-hand panel of Fig. 10, the positions of the peak are compatible within errorbars between the two cases.

Finally, we compute the position of the BAO feature in the bc-bc cross-correlation function from Fig. 9. In this case we use the same polynomial fitting formula (equation 9) but looking now for the minimum of our fit. As we mentioned before, results at low z become noisy which is why the errorbars on the peak position increase. The results are shown in the fourth column of Table 2. We do observe a somewhat higher value of the scale of the BAO dip with respect to that of the BAO peak of all other fields we consider (except haloes), which is expected as explained before.

To conclude, from Table 2, we do not detect any significant impact of relative baryon-CDM perturbations on the BAO peak position measured from the matter or halo correlation function. This is in line with results from the previous section where we found no evidence for a change in the broad-band correlation function from such perturbations. This is also again in line with previous results from Beutler et al. (2017) who found no evidence for non-zero bias parameters associated to these perturbations from the BOSS galaxy power spectrum. Furthermore, Barreira et al. (2020a) also forecasted that the BAO peak position should be shifted by less than 1 per cent for halo samples similar to the one we consider here (their section 4).

We end this section by a small word of caution. In this work, we only considered the effects of baryon-CDM relative perturbations generated by baryon–photon coupling prior to recombination. However, as we already mentioned in the introduction, compensated isocurvature perturbations (CIP) can also be generated in some Inflation scenarios. As was discussed in Heinrich & Schmittfull (2019), Barreira et al. (2020b), such CIPs can also locally affect the position of the BAO peak or the galaxy power spectrum, and these statistics could hence be used to constrain them as well as inflationary scenarios. A direct measurement of the impact of CIPs on the BAO peak position could be done using 1-fluid separate universe simulations as described in Barreira et al. (2020a), Khoraminezhad et al. (2021), but this is beyond the scope of this work.

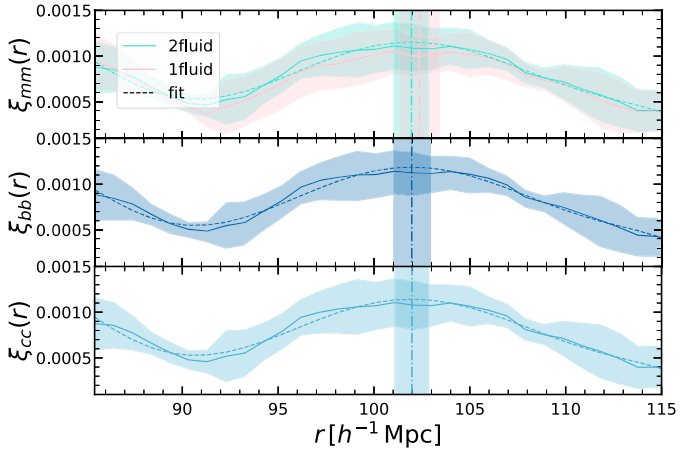

Figure 11. Top panel: Comparison between the matter–matter 2PCF in 1-fluid (pink) and 2-fluid (cyan) simulations. Middle and bottom panels: baryon–baryon and CDM–CDM 2-point correlation functions, respectively, in 2-fluid simulations. Each time we show the 2PCF in real space at $z = 0$, computed using equation (8). The shaded area show the 1σ error over eight realizations in each simulation. The vertical dotted-dashed lines show the position of the BAO peak obtained from a 7th degree polynomial fit of the form of equation (9). The polynomial fit is plotted in each case with the dashed line style and the same colour for each type of correlations. The position of the BAO peak in each case for all different redshifts are presented in Table 2.

Table 2. Position of the BAO peak of the halo and matter fields in 1-fluid and 2-fluid simulations for different redshifts. In the case of 2-fluid set, we also compute the position of the peak for CDM, baryons, and the δ_{bc} fields separately. We see that any shift in the peak position is within 1σ errorbars.

2fluid	Redshift	CDM	Baryon	δ_{bc}	Total matter	Halo ($12.45 < \log M < 12.95$)
	$z = 0$	102.0 ± 0.9	102.0 ± 1.0	102.3 ± 5.7	102.0 ± 0.9	101.2 ± 3.5
	$z = 0.5$	102.8 ± 1.5	102.8 ± 1.5	99.7 ± 7.5	102.9 ± 1.5	101.4 ± 1.8
	$z = 1$	102.9 ± 1.2	103.0 ± 1.1	105.2 ± 2.8	102.9 ± 1.2	104.5 ± 4.9
	$z = 1.5$	102.9 ± 0.9	102.9 ± 0.8	106.5 ± 2.0	102.9 ± 0.9	104.9 ± 2.3
	$z = 2$	102.7 ± 0.7	102.8 ± 0.7	104.7 ± 1.5	102.7 ± 0.7	107.4 ± 2.1
	$z = 3$	102.5 ± 0.5	102.5 ± 0.5	106.2 ± 2.6	102.5 ± 0.5	105.9 ± 2.8
1fluid	Redshift	CDM	Baryon	δ_{bc}	Total matter	Halo ($12.45 < \log M < 12.95$)
	$z = 0$	–	–	–	102.4 ± 1.0	99.1 ± 9.7
	$z = 0.5$	–	–	–	103.0 ± 1.8	102.2 ± 1.8
	$z = 1$	–	–	–	102.9 ± 1.2	101.9 ± 3.5
	$z = 1.5$	–	–	–	102.8 ± 0.8	104.9 ± 1.9
	$z = 2$	–	–	–	102.7 ± 0.7	105.6 ± 2.1
	$z = 3$	–	–	–	102.5 ± 0.5	106.4 ± 1.9

6 SUMMARY AND CONCLUSION

In this paper, we performed 2-fluid gravity-only simulations building on our previous work in Khoraminezhad et al. (2021), to study the impact of baryon-CDM relative perturbations due to photon pressure prior to recombination on voids statistics, density profile, and clustering, as well as the 2PCF and position of the BAO peak in real space of various fluid components. The main findings of this study can be summarized as follows:

(i) The VSF depends strongly on the tracer used to identify voids (there are more small voids and less large ones in the particle field than in the halo field). The VSF of particle field voids is unaffected by baryon-CDM relative perturbations, while the VSF of halo field voids is affected at $1 - 2$ per cent level: smaller voids are more abundant in presence of such perturbations and larger voids less, which is a consequence of the fact that these perturbations act against clustering (Fig. 1).

(ii) We did not detect any statistically significant impact of baryon-CDM relative perturbations on the void, matter or halo auto- and cross-2PCF. We found hints that these perturbations diminish the clustering on scales smaller than the BAO one, and enhance the BAO peak amplitude (Fig. 2, and Figs 8–10), which is in agreement with our expectations.

(iii) The density profiles of voids in halo and particle fields display the three known regimes (negative deep inside the void followed by the void profile regime with the positive compensation wall, and the linear regime where the halo–void correlation function becomes zero), and voids in the halo field are larger on average. We found no significant impact of baryon-CDM relative perturbations on any of the profiles, but a hint for voids in 2-fluid simulations to be emptier (Figs 3–5).

(iv) The void bias depends significantly on the tracer used to find voids (the bias is almost constant over void size for halo field voids but it decreases for larger voids in the particle field), but we found consistent results for bias obtained from cross- and autocorrelation functions. Again we did not find any significant difference for the bias in 1- and 2-fluid simulations, but found hints that it is slightly larger in the latter case, as we expect (Fig. 7).

(v) The amplitude of the BAO peak in the baryon 2PCF decreases with time due to gravitational evolution. It is gradually imprinted in

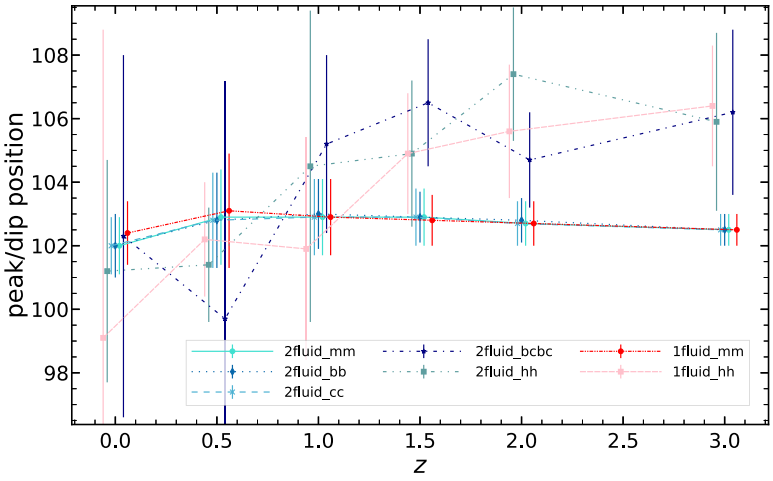

Figure 12. Position of the BAO peak (or dip) for 1- and 2-fluid simulations for different fields for different redshifts. These results correspond to those of Table 2. 2-fluid measurements are shown in nuances of blue according to the legend, and 1-fluid ones in red. We present the matter–matter case with circle markers and the halo–halo case with square markers. We see no statistically significant differences between these two cases. The points have been slightly displaced horizontally to increase clarity. Each field is shown with a different line style.

the CDM 2PCF where the amplitude of the peak grows down to $z \sim 7$ and then decreases down to $z = 0$ due to non-linear effects (Fig. 9).

(vi) The relative density perturbation δ_{bc} autocorrelation function presents a dip as BAO feature on scales slightly larger than the BAO peak, which is consistent with the fact that on these scales CDM particles lag behind baryons (Fig. 9).

(vii) We directly measured the impact that baryon-CDM perturbations have on the BAO peak position of halo and matter for the first time to our knowledge, and found no evidence for a statistically significant impact (Figs 11, 12 and Table 2), which is in agreement with previous works (Beutler et al. 2017).

The halo field VSF is the only quantity that we found to be affected with statistical significance by baryon-CDM relative perturbations due to photon pressure prior to recombination. This effect might hence also affect the VSF of voids obtained from galaxy fields in observational data, and this statistics could hence be used to constraint such perturbations. We note however that the effect remains quite small. Our results for the matter–matter and halo–halo 2PCF added to ones from previous works confirm that the impact of baryon-CDM perturbations on cosmological constraints from the BAO feature in current and future galaxy surveys should be negligible at low redshift ($z \leq 3$). This has important consequences for future galaxy clustering surveys since it means that these effects will not have to be included in the modelling of leading-order quantities used for the analysis of their data.

Finally, in the future, it would be interesting to use our extended set of simulations to reproduce the analysis in Khoraminezhad et al. (2021) including the two leading-order relative velocity bias parameters. This would allow us to constraint their amplitude and their impact on the galaxy power spectrum. It would also be interested to reproduce this study, at least partially, using separate universe simulations described in Barreira et al. (2020a) in order to measure the impact of CIPs generated during Inflation on voids statistics and BAO.

ACKNOWLEDGEMENTS

We thank Gabriele Parimbelli, Tommaso Ronconi, and Alexandre Barreira for useful discussions. HK, TL, MV, CB are supported by INFN INDARK grant. MV, CB also acknowledge contribution from the agreement ASI-INAF n.2017-14-H.0 and the ASI contracts Euclid-IC (I/031/10/0). CB, PV acknowledge support from the grant MIUR PRIN 2015 'Cosmology and Fundamental Physics: illuminating the Dark Universe with Euclid'. CB also acknowledges support from the ASI COSMOS and LiteBIRD Networks (cosmosnet.it).

DATA AVAILABILITY

The data underlying this article will be shared on reasonable request to the corresponding author.

REFERENCES

Ade P. A. R. et al., 2016, A&A, 594, A21
Aghanim N. et al., 2020, A&A, 641, A6
Ahn K., 2016, ApJ, 830, 68
Alam S. et al., 2021, Phys. Rev. D, 103, 083533
Alcock C., Paczynski B., 1979, Nature, 281, 358
Angulo R. E., Pontzen A., 2016, MNRAS, 462, L1
Angulo R. E., Hahn O., Abel T., 2013, MNRAS, 434, 1756
Anselmi S., Corasaniti P.-S., Starkman G. D., Sheth R. K., Zehavi I., 2018, Phys. Rev. D, 98, 023527
Baccigalupi C., 1999, Phys. Rev. D, 59, 123004
Baccigalupi C., Amendola L., Occhionero F., 1997, MNRAS, 288, 387
Baldi M., Villaescusa-Navarro F., 2018, MNRAS, 473, 3226
Barkana R., Loeb A., 2011, MNRAS, 415, 3113
Barreira A., Cautun M., Li B., Baugh C. M., Pascoli S., 2015, J. Cosmol. Astropart. Phys., 2015, 028
Barreira A., Cabass G., Nelson D., Schmidt F., 2020a, J. Cosmol. Astropart. Phys., 02, 005
Barreira A., Cabass G., Lozanov K. D., Schmidt F., 2020b, J. Cosmol. Astropart. Phys., 07, 049
Beutler F., Seljak U., Vlah Z., 2017, MNRAS, 470, 2723
Bird S., Feng Y., Pedersen C., Font-Ribera A., 2020, J. Cosmol. Astropart. Phys., 2020, 002
Blazek J., McEwen J. E., Hirata C. M., 2016, Phys. Rev. Lett., 116, 121303
Bos E. G. P., van de Weygaert R., Dolag K., Pettorino V., 2012, MNRAS, 426, 440
Cai Y.-C., Neyrinck M. C., Szapudi I., Cole S., Frenk C. S., 2014, ApJ, 786, 110

Cai Y.-C., Padilla N., Li B., 2015, MNRAS, 451, 1036
Cai Y.-C., Neyrinck M., Mao Q., Peacock J. A., Szapudi I., Berlind A. A., 2017, MNRAS, 466, 3364
Cautun M., van de Weygaert R., Jones B. J. T., Frenk C. S., 2014, MNRAS, 441, 2923
Ceccarelli L., Paz D., Lares M., Padilla N., Lambas D. G., 2013, MNRAS, 434, 1435
Chan K. C., Hamaus N., Desjacques V., 2014, Phys. Rev. D, 90, 103521
Chan K. C., Hamaus N., Biagetti M., 2019, Phys. Rev. D, 99, 121304
Chan K. C., Li Y., Biagetti M., Hamaus N., 2020, ApJ, 889, 89
Chen S.-F., Castorina E., White M., 2019, J.Cosmol. Astropart. Phys., 06, 006
Christopherson A. J., 2014, Int. J. Mod. Phys. D, 23, 1430024
Clampitt J., Cai Y.-C., Li B., 2013, MNRAS, 431, 749
Clampitt J., Jain B., Sánchez C., 2016, MNRAS, 456, 4425
Colberg J. M., Sheth R. K., Diaferio A., Gao L., Yoshida N., 2005, MNRAS, 360, 216
Contarini S., Ronconi T., Marulli F., Moscardini L., Veropalumbo A., Baldi M., 2019, MNRAS, 488, 3526
Contarini S., Marulli F., Moscardini L., Veropalumbo A., Giocoli C., Baldi M., 2021, MNRAS, 504, 5021
D'Amico G., Musso M., Noreña J., Paranjape A., 2011, Phys. Rev. D, 83, 023521
Dalal N., Pen U.-L., Seljak U., 2010, J. Cosmol. Astropart. Phys., 2010, 007
Davis M., Peebles P. J. E., 1983, ApJ, 267, 465
Desjacques V., Jeong D., Schmidt F., 2018, Phys. Rep., 733, 1
Falck B., Neyrinck M. C., 2015, MNRAS, 450, 3239
Ferrer F., Räsänen S., Väliviita J., 2004, J. Cosmol. Astropart. Phys., 2004, 010
Finelli F., García-Bellido J., Kovács A., Paci F., Szapudi I., 2014, Proc. IAU Symp. 10, Statistical Challenges in 21st Century Cosmology. Cambridge Univ. Press, Cambridge, p. 153
Furlanetto S. R., Piran T., 2006, MNRAS, 366, 467
Gibbons G. W., Werner M. C., Yoshida N., Chon S., 2014, MNRAS, 438, 1603
Gill S. P. D., Knebe A., Gibson B. K., 2004, MNRAS, 351, 399
Granett B. R., Neyrinck M. C., Szapudi I., 2008, ApJ, 683, L99
Granett B. R., Kovács A., Hawken A. J., 2015, MNRAS, 454, 2804
Gregory S. A., Thompson L. A., Tifft W. G., 1978, Bull. Am. Astron. Soc., 10, 622
Grin D., Doré O., Kamionkowski M., 2011, Phys. Rev. D, 84, 123003
Hahn O., Abel T., 2011, MNRAS, 415, 2101
Hahn O., Rampf C., Uhlemann C., 2021, MNRAS, 503, 426
Hamaus N. et al., 2022, A&A, 658, A20
Hamaus N., Sutter P. M., Wandelt B. D., 2014a, Phys. Rev. Lett., 112, 251302
Hamaus N., Wandelt B. D., Sutter P. M., Lavaux G., Warren M. S., 2014b, Phys. Rev. Lett., 112, 041304
Hamaus N., Sutter P. M., Lavaux G., Wandelt B. D., 2015, J. Cosmol. Astropart. Phys., 11, 036
Hamaus N., Pisani A., Sutter P. M., Lavaux G., Escoffier S., Wandelt B. D., Weller J., 2016, Phys. Rev. Lett., 117, 091302
Hamilton A. J. S., 1993, ApJ, 417, 19
Hand N., Feng Y., Beutler F., Li Y., Modi C., Seljak U., Slepian Z., 2018, AJ, 156, 160
Hang Q., Alam S., Cai Y.-C., Peacock J., 2021, MNRAS, 507, 510
Hausman M. A., Olson D. W., Roth B. D., 1983, ApJ, 270, 351
He C., Grin D., Hu W., 2015, Phys. Rev. D, 92, 063018
Heinrich C., Schmittfull M., 2019, Phys. Rev. D, 100, 063503
Hewett P. C., 1982, ApJ, 201, 867
Hotchkiss S., Nadathur S., Gottlöber S., Iliev I. T., Knebe A., Watson W. A., Yepes G., 2015, MNRAS, 446, 1321
Hotinli S. C., Mertens J. B., Johnson M. C., Kamionkowski M., 2019, Phys. Rev. D, 100, 103528
Huston I., Christopherson A. J., 2014, Isocurvature Perturbations and Reheating in Multi-Field Inflation. preprint (arXiv:1302.4298)
Iannuzzi F., Dolag K., 2011, MNRAS, 417, 2846
Jamieson D., Loverde M., 2019, Phys. Rev. D, 100, 123528
Jeffrey N. et al., 2021, MNRAS, 505, 4626
Khoraminezhad H., Lazeyras T., Angulo R. E., Hahn O., Viela M., 2021, J. Cosmol. Astropart. Phys., 03, 023
Kirshner R. P., Oemler A. J., Schechter P. L., Shectman S. A., 1981, ApJ, 248, L57
Knollmann S. R., Knebe A., 2009, ApJS, 182, 608
Kovac K. et al., 2013, MNRAS, 438, 717
Kovács A. et al., 2017, MNRAS, 465, 4166
Kovács A. et al., 2019, MNRAS, 484, 5267
Kreisch C. D., Pisani A., Carbone C., Liu J., Hawken A. J., Massara E., Spergel D. N., Wandelt B. D., 2019, MNRAS, 488, 4413
Landy S. D., Szalay A. S., 1993, ApJ, 412, 64
Langlois D., Riazuelo A., 2000, Phys. Rev. D, 62, 043504
Lavaux G., Wandelt B. D., 2010, MNRAS, 403, 1392
Lavaux G., Wandelt B. D., 2012, ApJ, 754, 109
Lewis A., Challinor A., Lasenby A., 2000, ApJ, 538, 473
Li B., 2011, MNRAS, 411, 2615
Li M., Lin C., Wang T., Wang Y., 2009, Phys. Rev. D, 79, 063526
Liddle A. R., Mazumdar A., 2000, Phys. Rev. D, 61, 123507
Linde A. D., Mukhanov V. F., 1997, Phys. Rev. D, 56, 535
Lyth D. H., Ungarelli C., Wands D., 2003, Phys. Rev. D, 67, 023503
Mao Q. et al., 2017, ApJ, 835, 161
Massara E., Villaescusa-Navarro F., Viel M., Sutter P. M., 2015, J. Cosmol. Astropart. Phys., 2015, 018
Michaux M., Hahn O., Rampf C., Angulo R. E., 2021, MNRAS, 500, 663
Nadathur S. et al., 2020, MNRAS, 499, 4140
Nadathur S., Crittenden R., 2016, ApJ, 830, L19
Nadathur S., Hotchkiss S., 2015, MNRAS, 454, 2228
Nadathur S., Lavinto M., Hotchkiss S., Räsänen S., 2014a, Phys. Rev. D, 90, 103510
Nadathur S., Hotchkiss S., Diego J. M., Iliev I. T., Gottlöber S., Watson W. A., Yepes G., 2014b, in Proc. IAU Symp. 308, Universal void density profiles from simulation and SDSS. Cambridge Univ. Press, Cambridge, p. 542
Neyrinck M. C., 2008, MNRAS, 386, 2101
Notari A., Riotto A., 2002, Nucl. Phys. B, 644, 371
O'Leary R. M., McQuinn M., 2012, ApJ, 760, 4
Obuljen A., Villaescusa-Navarro F., Castorina E., Viel M., 2017, J. Cosmol. Astropart. Phys., 2017, 012
Odrzywołek A., 2009, Phys. Rev. D, 80, 103515
Peebles P. J. E., Hauser M. G., 1974, ApJ, 28, 19
Peloso M., Pietroni M., Viel M., Villaescusa-Navarro F., 2015, J. Cosmol. Astropart. Phys., 2015, 001
Pezzotta A., Crocce M., Eggemeier A., Sánchez A. G., Scoccimarro R., 2021, Phys. Rev. D, 104, 043531
Philcox O. H. E., Ivanov M. M., Simonović M., Zaldarriaga M., 2020, J. Cosmol. Astropart. Phys., 2020, 032
Pisani A., Sutter P. M., Hamaus N., Alizadeh E., Biswas R., Wandelt B. D., Hirata C. M., 2015, Phys. Rev. D, 92, 083531
Platen E., van de Weygaert R., Jones B. J. T., 2007, MNRAS, 380, 551
Platen E., van de Weygaert R., Jones B. J. T., 2008, MNRAS, 387, 128
Polarski D., Starobinsky A. A., 1994, Phys. Rev. D, 50, 6123
Pollina G., Baldi M., Marulli F., Moscardini L., 2016, MNRAS, 455, 3075
Pollina G., Hamaus N., Dolag K., Weller J., Baldi M., Moscardini L., 2017, MNRAS, 469, 787
Raghunathan S., Nadathur S., Sherwin B. D., Whitehorn N., 2020, ApJ, 890, 168
Rampf C., Uhlemann C., Hahn O., 2021, MNRAS, 503, 406
Rees M. J., Sciama D. W., Stobbs S. H., 1968, Astrophys. Lett., 2, 243
Ricciardelli E., Quilis V., Planelles S., 2013, MNRAS, 434, 1192
Ricciardelli E., Quilis V., Varela J., 2014, MNRAS, 440, 601
Schaap W. E., 2007, PhD Thesis, University of Groningen
Schmidt F., 2016, Phys. Rev. D, 94, 063508
Schmidt F., 2021, J. Cosmol. Astropart. Phys., 04, 032
Schuster N., Hamaus N., Pisani A., Carbone C., Kreisch C. D., Pollina G., Weller J., 2019, J. Cosmol. Astropart. Phys., 2019, 055
Sheth R. K., van de Weygaert R., 2004, MNRAS, 350, 517
Slepian Z. et al., 2018, MNRAS, 474, 2109
Slepian Z., Eisenstein D. J., 2015, MNRAS, 448, 9

Springel V., 2005, MNRAS, 364, 1105
Sutter P. M., Lavaux G., Wandelt B. D., Weinberg D. H., 2012, ApJ, 761, 187
Sutter P. M., Lavaux G., Hamaus N., Wandelt B. D., Weinberg D. H., Warren M. S., 2014a, MNRAS, 442, 462
Sutter P. M., Pisani A., Wandelt B. D., Weinberg D. H., 2014b, MNRAS, 443, 2983
Taruya A., Nishimichi T., Saito S., Hiramatsu T., 2009, Phys. Rev. D, 80 , 123503
Tinker J. L., Robertson B. E., Kravtsov A. V., Klypin A., Warren M. S., Yepes G., Gottlöber S., 2010, ApJ, 724, 878
Tseliakhovich D., Hirata C., 2010, Phys. Rev. D, 82, 083520
Väliviita J., Savelainen M., Talvitie M., Kurki-Suonio H., Rusak S., 2012, ApJ, 753, 151
Verza G., Pisani A., Carbone C., Hamaus N., Guzzo L., 2019, J. Cosmol. Astropart. Phys., 2019, 040
Viel M., Colberg J. M., Kim T.-S., 2008, MNRAS, 386, 1285
Vielzeuf P. et al., 2021, MNRAS, 500, 464
Villaescusa-Navarro F., Alonso D., Viel M., 2017, MNRAS, 466, 2736
Yoo J., Seljak U., 2013, Phys. Rev. D, 88, 103520
Yoo J., Dalal N., Seljak U., 2011, J. Cosmol. Astropart. Phys., 2011, 018
Yoshida N., Sugiyama N., Hernquist L., 2003, MNRAS, 344, 481
Zeldovich Y. B., 1970, A&A, 500, 13
Zivick P., Sutter P. M., Wandelt B. D., Li B., Lam T. Y., 2015, MNRAS, 451, 4215

This paper has been typeset from a TEX/LATEX file prepared by the author.